Biointerface Research in Applied Chemistry
Open-Access Journal (ISSN: 2069-5837)

Article
Volume 16, Issue 1, 2026, 40
https://doi.org/10.33263/BRIAC161.040

Combined Semi-empirical Docking, QSAR, Molecular Dynamics, and DFT Studies for Identifying Potential Anticancer Agents in Royal Jelly

Yelin Adalina [1], Gusnia Meilin Gholam [1,2], Dimas Andrianto [2], Siti Sumiati Solihat [1,2], Christofora Hanny Wijaya [3], Araz Meilin [4], Totok Kartono Waluyo [1], Rohmah Pari [1], Ina Winarni [5], I Made Artika [2,*]

[1] Research Center for Applied Botany, National Research and Innovation Agency (BRIN), Jl. Raya Jakarta-Bogor Km. 46, Cibinong, Bogor, Jawa Barat - 16911, Indonesia
[2] Department of Biochemistry, Faculty of Mathematics and Natural Sciences, IPB University, Dramaga Campus, Bogor, 16680, Indonesia
[3] Department of Food Science and Technology, Faculty of Agricultural Engineering, IPB University, Dramaga, Indonesia
[4] Research Center for Horticulture, National Research and Innovation Agency, Cibinong, Bogor, West Java, 16911, Indonesia
[5] Research Center for Biomass and Bioproducts, Research Organization for Life Sciences and Environment, National Research and Innovation Agency (BRIN), Bogor 16911, Indonesia
* Correspondence: imart@apps.ipb.ac.id;

Received: 8.06.2025; Accepted: 13.01.2026; Published: 15.02.2026

Abstract: Cancer rates are expected to increase, with Src kinase playing a crucial role in cancer metabolism. This study explored bioactive compounds in royal jelly (RJ) as novel anticancer agents targeting Src kinase using computational methods. QM-AM1 was used for structure preparation, while MD simulations assessed protein-ligand stability, and advanced analyses provided post-MD data. The results indicated that, among the bioactive compounds in RJ, formononetin was promising, with a binding energy of 8.243 kcal/mol and interactions with the active sites of two Src kinase pockets. DFT calculations for formononetin suggested good stability and low reactivity. MD simulations demonstrated that the Src kinase–Formononetin complex adopted a stable, favorable binding pose, and subsequent MM-PBSA analysis indicated a markedly stronger binding affinity than that of the reference inhibitor AP23451. PCA analysis revealed overlapping energy distributions and a positive correlation between RMSDca and DCCM plots, providing insights into the stability and conformation of the Src kinase-formononetin complex. This study proposes formononetin as a novel anticancer inhibitor candidate through comprehensive *in silico* computational analysis, while acknowledging that further validation through *in vitro* and *in vivo* studies is required.

Keywords: cancer; computational; Src kinase; principal component analysis; HOMO-LUMO; royal jelly.

1. Introduction

Cancer, a multifactorial disease occurring at the molecular level, leads to uncontrolled cell growth. Cancer onset can drastically weaken the immune system and exploit the physiology of other cells in the body. This process is typically triggered by the accumulation

of genetic mutations that disrupt the regulation of the cell cycle, apoptosis, and DNA repair mechanisms. As a result, cancer cells rapidly proliferate, evade immune system control, and have the potential to spread to other parts of the body through metastasis [1]. Cancer can affect all types of cells in the body and target various organs [2]. In 2022, there were 19,98 million new cancer cases diagnosed globally, along with 9,74 million cancer-related deaths, and this number is expected to increase in the future due to aging populations and lifestyle changes [3].

Cancer metabolism is characterized by increased glucose uptake, activation of specific enzymes, and fatty acid synthesis, all of which help cancer cells meet their energy requirements and support cell proliferation. Furthermore, cancer metabolism is associated with cancer cells' ability to evade immune detection and destruction[4]. Enzymatic metabolism plays a critical role in the production of amino acids, fatty acids, and nucleotides, which are essential for cell survival. Dysregulated enzyme metabolism in cancer cells contributes to resistance to apoptosis [5]. One of the enzymes that plays a significant role in cancer progression is Sarcoma (Src) kinase, which, when overexpressed, can accelerate cancer development [6]. Activation of Src kinase has been linked to various types of cancer, including brain cancer, glioblastoma, liver cancer, lung cancer, colorectal cancer, breast cancer, bladder cancer, and pancreatic cancer [7].

Src family kinases (SFKs) are non-receptor tyrosine kinases involved in the regulation of crucial cellular functions, such as cell proliferation, differentiation, apoptosis, migration, and metabolism. The Src kinase family in vertebrates consists of nine members: Src, Lymphocyte cell-specific protein tyrosine kinase (LCK), Lck-related novel protein tyrosine kinase (LYN), B lymphoid tyrosine kinase (BLK), Hemopoietic cell kinase (HCK), Fyn proto-oncogene (FYN), Feline sarcoma viral protein Gardner-Rasheed (FGR), YES, and YRK [8]. Src, FYN, and YES are widely expressed in mammals, whereas LYN and FGR are expressed in the hematopoietic system, HCK is expressed in myeloid lineage cells, BLK is expressed in B cells, and LCK is expressed in T cells [9]. Src kinase plays a pivotal role in cancer initiation through the tyrosine phosphorylation of various protein substrates [10].

Src kinase has recently emerged as a key target for the development of cancer therapies. Inhibition of Src kinase has shown minimal toxicity and plays a role in suppressing the growth of colorectal cancer cells [11]. Zhang and Yu [12] ported that targeting the Src kinase in cancer therapy could restore immune responses mediated by cytotoxic T cells. Moreover, Src kinase signaling can enhance B-cell receptor signaling, which can inhibit apoptosis signaling in cancer. Src kinase inhibition can neutralize mechanisms that induce phenotypic changes driven by cancer stimulants, angiogenesis, and immune system infections [13].

Cancer treatment continues to be actively pursued through both conventional and modern approaches. Conventional treatment involves surgery and medication; however, these methods are considered ineffective because they can damage healthy cells. On the other hand, modern treatments involve cell therapy and targeted drug therapies that focus on molecular mechanisms. These cancer treatment methods are considered more precise and tend to causeewer side effects [14]. Additionally, cancer treatment is also carried out with the use of herbal medicines. Herbal remedies with anti-cancer effects are favored due to their low toxicity and their ability to inhibit apoptosis induction [15]. For instance, research by Lee *et al*. [16] revealed that gallic ac, found in plants and fruits, can act as an inhibitor of Src kinase signaling and an activator of the STAT3 transcription signaling pathway.

Another example of a herbal substance used in cancer treatment is RJ. RJ is known for its anti-cancer properties, particularly due to its phytochemical content, includinglavonoids [17]. RJ is a gelatinous substance produced by the mandibular and hypopharyngeal glands of

worker bees. It contains carbohydrates, proteins, peptides, lipids, vitamins, and minerals [18]. RJ has been a part of Chinese culture since ancient times and is recognized as a component of Traditional Chinese Medicine (TCM). It is widely used in traditional therapies, dietary supplements, and cosmetic formulations. RJ's bioactive properties contribute to reproductive health, enhance memory, help prevent dementia, and even reduce anxiety [19–22]. Sönmez [23] has elucidated that RJ is compositionally complex. RJ was selected as the primary sample because of its exceptionally rich composition of bioactive constituents, including major royal jelly proteins (MRJPs), 10-HDA, flavonoids, and phenolic compounds, which collectively contribute to its broad pharmacological profile. This profile encompasses antimicrobial, antioxidant, anti-inflammatory, immunomodulatory, anticancer, and wound-healing activities. Key molecules, such as 10-HDA and MRJPs, have been consistently identified as critical drivers of RJ's anti-aging, regenerative, and antitumor effects, indicating strong therapeutic relevance. Furthermore, RJ has demonstrated the capacity to modulate the gut microbiota and mitigate inflammatory and autoimmune responses, further substantiating its biomedical potential. Given this diverse and potent spectrum of biological activities, which is supported by substantial preclinical evidence, the selection of RJ as a bioactive source for inhibitor screening is scientifically justified. This is particularly true for the identification of multifunctional compounds relevant to targeted molecular interventions.

The use of herbal substances as anti-cancer agents is widespread; however, specific targeting of Src kinase for cancer treatment remains rare. This study aimed to explore cancer treatment targeting the Src kinase protein using bioactive compounds from RJ. To date, no bioactive compounds in RJ that can inhibit Src kinase have been identified. This study hypothesized that RJ may have a direct effect in inhibiting cancer growth driven by Src kinase. Therefore, the goal of this study was to conduct a computational investigation of bioactive compounds in RJ that target Src kinase, with the aim of proposing a new cancer treatment agent.

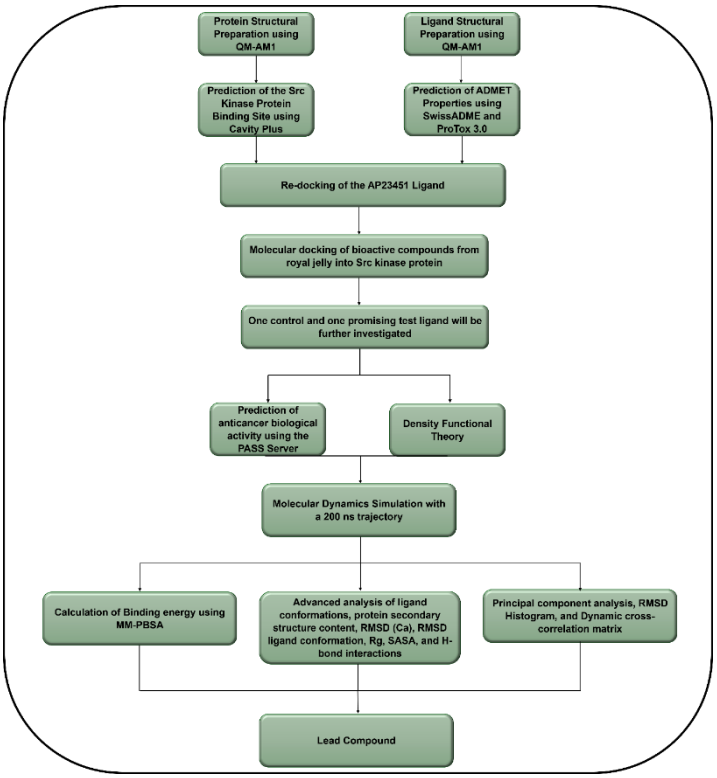

Figure 1. Workflow of this study for proposing Src kinase protein inhibitor candidates as new anticancer agents.

This study focused on a comprehensive *in silico* computational approach to evaluate various compounds contained in RJ as candidate Src kinase protein inhibitors. The research employs multiple *in silico* computational techniques, including quantum mechanics (QM) applications, Src kinase protein active site prediction, absorption, distribution, metabolism, excretion, and toxicity (ADMET) profiling, molecular docking, prediction of activity spectra for substances (PASS) prediction to assess anticancer biological activity, density functional theory (DFT) calculations, and molecular dynamics (MD) simulations. These techniques were comprehensively applied to evaluate potential Src kinase-ligand complexes. Based on these methodologies, this study proposes potential Src kinase inhibitors, suggesting them as promising anticancer agents for preliminary screening (early-stage prediction in the drug discovery process for target receptor inhibitors). The entire workflow of this study is presented in Figure 1.

2. Materials and Methods

2.1. Protein structural preparation.

This study uses the Src kinase protein deposited in the RCSB PDB with the code 2BDF (rcsb.org/structure/2BDF). The Src kinase protein has a resolution of 2.10 Å and is bound to the inhibitor AP23451 (referred to as the control inhibitor). We then downloaded it from (.pdb) format, and saved it in our working directory. For the structural preparation of the Src kinase protein, we used YASARA Structure (Version 19.9.17), paying careful attention to several settings. The Src kinase protein is surrounded by water molecules, which were removed during the preparation process in the YASARA Structure. The environmental conditions for Src kinase were adjusted by adding hydrogen atoms and setting the pH to 7.5. We selected the AM1 quantum mechanics (QM-AM1) method along with energy minimization. The bound inhibitor, AP23451, was then separated into (.sdf) format to assist in the redocking process. The prepared Src kinase protein was saved in (.yob) and (.pdb) format for subsequent analysis. We analyzed the overall quality of the Src kinase protein using the Ramachandran plot and Verify 3D through SAVES (saves.mbi.ucla.edu/ - Version 6.1) and continued quality analysis using ProSA-web (Protein Structure Analysis – prosa.services.came.sbg.ac.at/prosa.php). For each of these servers, we uploaded the (.pdb) format to run the analysis [24–28].

2.2. Ligand structural preparation.

The list of bioactive compounds identified from royal jelly was obtained from studies by El-Seedi *et al*. [29] and Botezan *et al* [30]. The reference ligand used in this study was obtained from Khamouli *et al*. [24], named CID_70144047 (referred to as the reference control). From this list, we obtained the ligand structures via PubChem (pubchem.ncbi.nlm.nih.gov/) and downloaded the individual ligand structures in (.sdf) format. The downloaded ligands were saved in our working directory for structural preparation using YASARA Structure. Each ligand was individually prepared by adding hydrogen atoms and applying QM-AM1. Subsequently, each ligand underwent energy minimization and was saved in (.pdb) format. These individual ligand preparations were then combined into a single file with the control drug and reference control in (*ligands.sdf) format for molecular docking [31–34].

2.3. Prediction of Src kinase protein binding sites.

We identified the amino acid residues where ligands interact using Cavity Plus 2022 (pkumdl.cn:8000/cavityplus#/). During the running process, the previously prepared Src kinase protein in (.pdb) format was uploaded to the server. We selected chain A of the Src kinase protein to ensure that it was not in ligand mode. Cavity Plus 2022 provided visualizations of the detection areas in terms of predicted maximal pKd (Pred Max pKd), predicted average pKd (Pred Ave pKd), drugScore, druggability, surface area, volume, and box size. Other settings were kept as default in accordance with Cavity Plus 2022 conditions [35].

2.4. Prediction of ADMET properties.

In drug discovery and candidate selection, pharmacokinetic properties are crucial. These provide insights into the proposed compounds and correlate with in silico predictions through human clinical trials, simulating a chemical species similar to a drug. In this study, the absorption, distribution, metabolism, excretion, and toxicity (ADMET) predictions for the test ligands were based on the SMILES notation of each individual ligand. SMILES for each ligand were obtained from PubChem. The SwissADME database (swissadme.ch/) was used to evaluate the physicochemical properties, pharmacokinetic profiles, drug-likeness, medicinal chemistry, and water solubility of the compounds, while ProTox 3.0 (tox-new.charite.de/protox_II/) was used to assess oral toxicity predictions [36–37].

2.5. Molecular docking.

The compound AP23451 bound to the Src kinase protein was released and saved in (*ligand.sdf) format to assist with the re-docking process. This allowed us to determine an appropriate grid box size based on the RMSD values. Grid box validation was performed using YASARA Structure. During this validation, we used grid box sizes of 1, 2.5, 5, 7.5, and 10 Å to obtain the smallest RMSD value. For re-docking, we used the dock_run.mcr macro with 25 runs and applied the VINA-based method. We then calculated the RMSD to ensure it was less than 2 Å. The molecular docking process proceeded after identifying the grid box size with the smallest RMSD. Molecular docking was performed again using the VINA-based method with 25 runs. QM-AM1 was applied to aid the molecular docking process. The Src kinase protein containing the AP23451 compound in (.yob) format was uploaded into YASARA Structure, and we adjusted the grid box size based on the validation results. Then, the Src kinase protein was set to a rigid conformation, with the AP23451 compound removed, and saved in (*receptor.sce) format. The file containing the test compounds and the control inhibitor in (*ligands.sdf) format was uploaded and saved in (*complex.sce) format. Finally, the docking process was run using the dock_runscreening.mcr script. To rank the binding energies, we used kcal/mol, with more positive values indicating strong binding of the compound to Src kinase [31–34]. For the post-docking visualization and data analysis, we used BIOVIA Discovery Studio (Version 2024).

2.6. PASS activity prediction.

To predict the biological activity properties relevant to cancer treatment, we used PASS (way2drug.com/passonline/). Predictions were made based on the previously stored SMILES notations. The PASS server evaluates compounds based on their Pa (probability of activity)

and Pi (probability of inactivity) values. A compound is considered biologically active if the Pa value is greater than the Pi value, indicating a predicted biological activity [38-39].

2.7. Frontier molecular orbitals calculation.

The selected test compounds, along with one of the controls, were then subjected to density functional theory (DFT) calculations using ORCA (Version 5). The compounds analyzed were the ones that had undergone structural preparation. Each compound was prepared individually in Avogadro, and the ORCA input was generated. The frontier molecular orbitals (FMO) calculations were based on the B3LYP/def2-SVP method. Additionally, molecular properties such as chemical potential (μ), ionization potential (I), electronegativity (χ), electron affinity (A), softness (S), hardness (η), and electrophilicity index (ω) were also calculated. These molecular properties were determined based on the HOMO (highest occupied molecular orbital) energy and the LUMO (lowest unoccupied molecular orbital) energy. The energy gap was calculated using the following equation [40,41]:

$$E_{HOMO} - E_{LUMO} \quad (1)$$

Electron affinity (A) (2):

$$A = -E_{LUMO} \quad (2)$$

Ionization potential (I) (3):

$$I = -E_{HOMO} \quad (3)$$

Chemical potentials (4):

$$-\frac{(I + A)}{2} \quad (4)$$

Electronegativity (χ) (5):

$$\frac{(I + A)}{2} \quad (5)$$

Softness (6):

$$\frac{1}{2\eta} \quad (6)$$

Hardsness (7):

$$\frac{(I - A)}{2} \quad (7)$$

Electrophilicity index (8):

$$\frac{\mu 2}{2\eta} \quad (8)$$

2.8. Molecular dynamics simulation.

We simulated the protein-ligand complex using molecular dynamics (MD) in YASARA Structure, by considering some settings before the process runs. The protein-ligand complex was run for 200 ns with an environment set to pH 7.4, a physiological solution containing 0.9% NaCl, and a water density of 0.997 g/ml. In the context of cancer studies, a simulation time of 200 ns represents a robust choice for binding energy calculations and post-MD analysis [42]. The energy minimization of the protein-ligand complex was completed by YASARA Structure. QM-AM1 was applied to the protein-ligand complex. The simulation was performed at a temperature of 310 K with pressure control mode activated by removing the "#" sign. This study employs a temperature of 310 K, as anticancer research by Rathod *et al*. has optimized and established this physiological body temperature as the most suitable condition for such simulations [43]. The entire trajectory production was saved in "sim" format, and the cell was extended by 10 Å around the solute. In the trajectory production, the complex was set

to save simulation snapshots every 250,000 fs. These settings were assisted and executed by the macro file md_run.mcr. Next, to analyze the advanced post-MD calculations, which include root mean square deviation of C-alpha (RMSDCa), root mean square deviation of ligand conformation (RMSDLc), protein secondary structure content, radius of gyration (Rg), solvent accessible surface area (SASA), and H-bonds, we used two macros: md and md_analyze. Specifically, for calculating the root mean square fluctuations (RMSF), we used the macro md_analyzeres. To process the resulting big data, this study utilized Microsoft Excel (Version 2511) and Notepad++ (Version 8.7.5). RMSD, RMSF, and Rg were calculated using the equations provided by YASARA Structure [31–34]:

RMSD:

$$\text{RMSD}=\sqrt{\frac{\sum_{i=1}^{n} R_i * R_i}{n}} \quad (9)$$

Ri is a vector connecting the positions of I atoms (of N atoms) in the reference snapshot and the current snapshot after the optimal superposition [31–33].

$$\text{RMSF: } \sqrt{\sum_{j=1}^{3}\left(\frac{1}{N}\sum_{k=1}^{N} P_{ij}^{2}\right)} \quad (10)$$

The RMSF of the atom *I* with *j* from 1 to 3 for the x, y, and z coordinates of the position vector *P* of the atom and *k* over the set of *N* evaluated snapshots was calculated [31–33].

Rg:

$$\text{Radius}_{\text{gyr, Mass}}=\sqrt{\frac{\sum_{i=1}^{N} \text{Mass}_i(\vec{R}_i-\vec{C})^2}{\sum_{i=1}^{N} \text{Mass}_i}} \quad (11)$$

In the formula, C is the center of mass, and Ri is the position of the i atom of N [32–34].

2.9. Calculation of binding energy through MM-PBSA.

The binding energy of the protein-ligand complex post-MD was calculated using molecular mechanics Poisson–Boltzmann surface area (MM-PBSA) as the scoring function in computational drug design. The MM-PBSA calculation was performed through the macro md_analyzebindenergy using the following equation [32–34]:

$$\text{Binding Energy} = E_{\text{potRecept}} + E_{\text{solvRecept}} + E_{\text{potLigand}} + E_{\text{solvLigand}} - E_{\text{potComplex}} - E_{\text{solvComplex}} \quad (12)$$

2.10. Principal component analysis.

Principal component analysis (PCA) was carried out using the Bio3D package in R programming with the function “mktrj.pca.” PCA helped us in performing a multivariate analysis to explore the distribution within the protein-ligand complex [44]. The mathematical equation for PCA is as follows:

$$X = T_K P_K^T + E \quad (13)$$

Where X matrix defines the product of two new matrices, i.e., Tk and Pk, Tk defines the score of the matrix indicating how samples correlate to each other, Pk defines the matrix of loadings which enclose data about how variables correlate to each other, k defines the total factors involved in the model, and E defines the matrix of residuals [45].

2.11. RMSD histogram analysis.

We calculated the RMSD histogram based on the 200 ns trajectory data of the protein-ligand complex using the Bio3D package in R programming (Version 4.4.2) via the function “rmsd()” [46].

2.12. Dynamics cross-correlation matrix.

The 200 ns trajectory data of the protein-ligand complex were analyzed for the dynamics cross-correlation matrix (DCCM) using the Bio3D package in R programming [46]. DCCM provides insights into the cross-correlation analysis within the protein-ligand complex. DCCM was run using the "dccm()" function, and the calculations were based on the following formula:

$$DCCM_{ij} = \frac{\langle \vec{di}.\vec{dj} \rangle}{\sqrt{\langle di^2 \rangle \langle dj^2 \rangle}} \quad (14)$$

Where the values di and dj indicate the displacement from the initial position relative to the average site position, the DCCMij value is represented from 1 to -1. Positive correlation at each atom indicates parallel interactions, while negative correlation indicates antiparallel interactions between Cα atoms and other atoms in the protein structure [32–34].

3. Results and Discussion

Here, we present a comprehensive *in silico* investigation to identify potential inhibitor candidates targeting the Src kinase protein as novel anticancer agents. Comprehensive *in silico* computations have been widely used to identify new drug candidates for various diseases detrimental to human health. In contexts like the one explored in this research, *in silico* approaches have been extensively applied to suggest drug candidates for breast cancer, lung cancer, oral cancer, prostate cancer, and cervical cancer [47–51].

3.1. Post-preparation protein.

To ensure the Src kinase protein met high-quality standards suitable for further molecular docking studies, we evaluated its quality using several assessment parameters: the Ramachandran plot, Verify 3D, Z-score, and local model quality. Figure 2A shows the results of the Ramachandran plot, with 81.4% of residues in the most favored regions, 15.9% in additional allowed regions, 0.4% in generously allowed regions, and 2.2% in disallowed regions. These results indicate that the percentage of residues in the most favored regions is significantly higher than that in the disallowed regions, meeting the criteria for high-quality protein. Additionally, the percentage of residues in the most favored regions above 80% correlates with the results in Figure 2B, which show that the Src kinase protein we prepared passed the Verify 3D evaluation, with 83.52% of residues having an average 3D-1D score≥ 0.1. Positive results are also reflected in Figure 2C, which indicates the overall model quality of Src kinase with a Z-score of -7.31. For local model quality, the energy map based on the amino acid sequence position of the Src kinase protein is in the knowledge-based energy area, below 0.0 (Figure 2D). Finally, we observed that the quality of the prepared Src kinase protein in this study was excellent, ensuring that the research was conducted with a protein of standardized quality, as verified by PROCHECK and ProSA-WEB evaluations.

In this study, we analyzed the quality of the Src kinase protein that we prepared. Proteins are fundamental components of life, and understanding their 3D structure can significantly help in understanding their biological, physical, and biochemical properties [52]. In the protein preparation stage, we introduced the Ramachandran plot, as this parameter has been extensively used in research to assess the quality of a target protein/enzyme. For example, in a study on prostate cancer that modeled the complete HOXB13 protein using MODELLER, the HOXB13 protein model was evaluated for quality using the Ramachandran plot [53].

Another study by Khater and Nassar on tertiary structure prediction and validation also employed the Ramachandran plot. The Ramachandran plot is commonly used to provide visual feedback and evaluate the rationality of a protein structure [54-55]. In our study, we found that the Src kinase protein we prepared was in good condition based on our overall analysis.

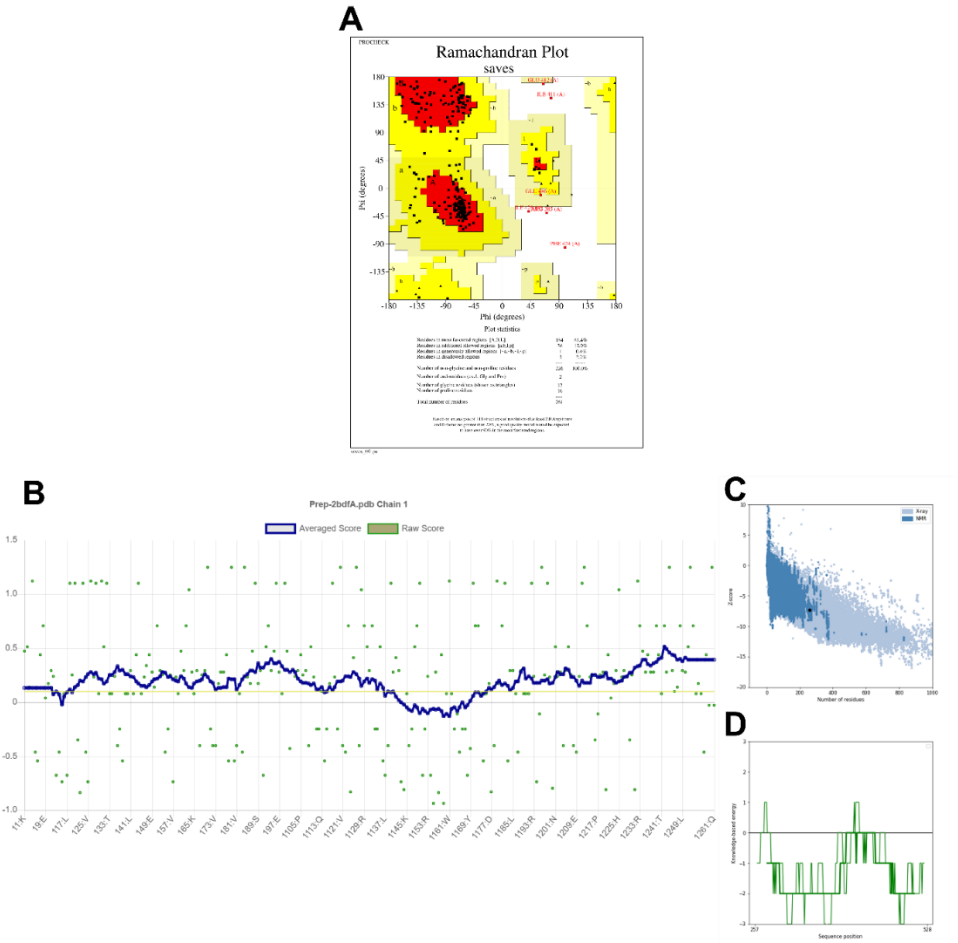

Figure 2. Assessment of Src kinase protein quality in protein preparations using YASARA structure. **(a)** Ramachandran plot; **(b)** Verify3D; **(c)** Overall model quality; **(d)** Local model quality

3.2. Prediction of Src kinase protein binding site.

To identify and evaluate potential binding sites in the Src kinase protein for drug design, we conducted an analysis to expand the pockets that could accommodate candidate compounds, enabling them to interact optimally with the protein in its functional state. Based on the Cavity Plus identification, we identified at least three potential pockets. However, upon further analysis, we found that only two of these pockets met the criteria for good pockets. As shown in Table 1, pocket 1 ranks highest, with a sufficiently large box size of 21.0 × 16.5 × 15.5 Å. With this box size, the calculated surface area is 838.25 Å², and within this pocket, we identified 64 amino acid residues. The characteristics of this pocket are classified as strong, with a drug score of 1839.00 and a druggability score in the strong range. The drug score for pocket 1 is a key factor in assessing the pocket, as the drug score for pocket 2 is lower, at 1342.00, although druggability remains strong (Figure 3A). Pocket 2 has a surface area of 871.50 Å² and a box size of 24.0 × 17.0 × 15.5 Å. This is shown in Figure 3B, where the pocket area appears larger compared to pocket 1. This observation aligns with the surface area and box size values, where pocket 1 has a larger surface area and box size than pocket 2. Pocket 3, on the other hand, exhibits a significantly low drug score of –441.00, correlating with weak

druggability. Additionally, the surface area and volume values are also low for this pocket, making it unsuitable for use. The list of potential amino acid residues, along with the secondary structure positions of Src kinase (Figure 3C) and a 3D visual representation of the pocket, is presented in Figure 3. Therefore, the identified potential cavities may be valuable for further studies in this research to explore the interactions between compounds and the Src kinase protein.

Table 1. Predicted Src kinase protein-binding site using CavityPlus.

Rank	Pred max pKd	Pred ave pKd	DrugScore	Druggability	Surface area (Å^2)	Volume (Å^3)	Box size (Å)
1	10.21	6.92	1839.00	Strong	838.25	1529.62	21.0; 16.5; 15.5
2	11.08	6.98	1342.00	Strong	871.50	1447.75	24.0; 17.0; 15.5
3	7.13	5.06	–441.00	Weak	206.00	193.38	10.0; 10.5; 9.0

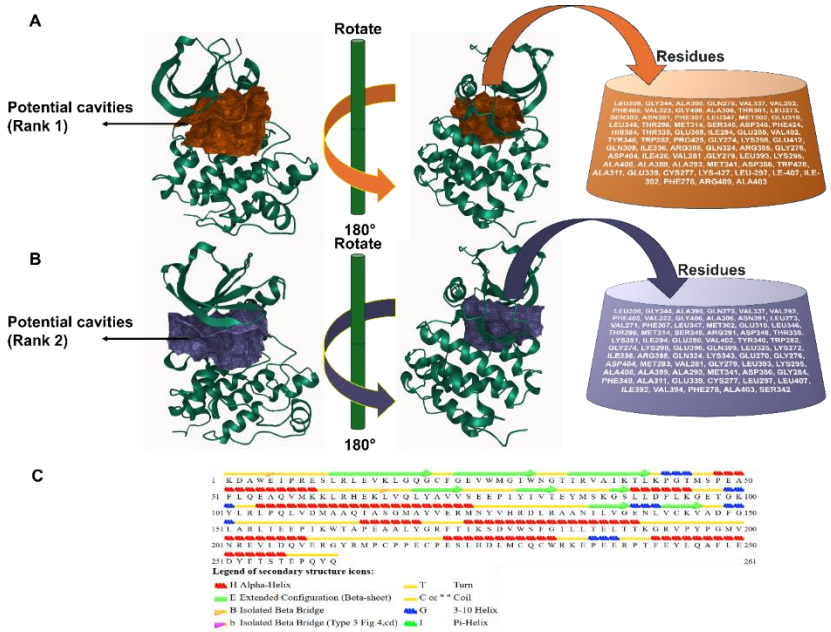

Figure 3. Binding site pocket analysis of the Src kinase protein using CavityPlus. **(a)** Rank 1 potential binding-site pocket of Src kinase; **(b)** Rank 2 potential binding-site pocket of Src kinase; **(c)** Secondary structure of the Src kinase protein.

In addition to evaluating the quality of the Src kinase protein, we provided insights into predicting its binding sites. A protein's function is closely linked to its binding sites on its surface [56]. In our research, we identified at least three pockets that interact with test compounds within the Src kinase protein. Among these three pockets, we conducted a more detailed analysis of those with favorable drug scores and druggability. This led to the hypothesis that structure-based drug development targeting Src kinase could interact with these predicted binding pockets. Two of the pockets successfully predicted in this study were identified as active sites suitable for drug targeting, based on their highest drug score through CavityPlus [52,53]. In anticancer research, Venkatesh et al. [57] reported using cavity analysis to assist in post-docking procedures for examining ligand-receptor interactions. Specifically, CavityPlus was employed prior to molecular docking to identify the active sites on 3ERT and 5UGB. Several approaches exist for applying CavityPlus to determine the location and geometry of binding pockets and to provide supplementary active-site predictions within a study.

3.3. ADMET analysis.

To evaluate the pharmacokinetics of the test compounds from royal jelly (RJ), we performed ADMET analysis. The results are presented in Table 2. Based on predictions from SwissADME and ProTox, we identified two compounds with relatively high molecular weights, namely naringin (molecular weight 580.53 g/mol) and chlorogenic acid (molecular weight 354.31 g/mol). However, other test compounds had molecular weights ranging from 70.67 to 302.28 g/mol. This molecular weight correlates with pharmacokinetic properties, specifically gastrointestinal absorption (GI absorption). The two compounds with higher molecular weights exhibited lower GI absorption. Surprisingly, druglikeness analysis using Lipinski's rule indicated that only naringin failed to meet the druglikeness criteria. This finding is noteworthy, as the SwissADME predictions helped filter out compounds that were less likely to be suitable for further testing. Toxicity screening using ProTox indicated the LD50 values and predicted the toxicity class. The predicted toxicity class in category 5 was still considered acceptable, whereas classes 1, 2, 3, and 4 were considered intolerable. Based on the ADMET analysis, we performed molecular docking tests, using the ADMET results to filter compounds predicted to perform poorly.

Computational *in silico* research aims to discover and propose potential drug candidates that are predicted to enhance effectiveness, efficiency, and even shorten drug development timelines [58]. In this study, we also provided predictions of the ADMET properties. ADMET properties have been widely used to predict drug bioavailability and other physicochemical properties. These predictions serve as the initial and crucial steps in supporting drug discovery and development. Ideally, a high-quality drug should have sufficient efficacy against its therapeutic target, along with ADMET properties that align with the therapeutic dose. Additionally, this research helped us select compounds predicted to meet ADMET parameters [59]. Thus, only compounds that met the necessary criteria and showed inhibitory activity and interaction with the Src kinase protein target were considered. To date, researchers still rely on the ADMET approach because the biological activity of test compounds must be balanced with minimized toxicity by first predicting compounds with low toxicity. It has also been shown that early-stage ADME estimations in the discovery phase help drastically reduce pharmacokinetic failure rates in clinical drug development trials [60].

Table 2. ADMET predictions for all test compounds from royal jelly.

Compound	Physicochemical properties			Lipophilicity		Pharmacokinetics	Druglikeness	Medicinal chemistry	Oral toxicity	
	Formula	Molecular weight (g/mol)	TPSA (Å²)	Consensus Log $P_{o/w}$	Log *S* (ESOL)	GI absorption	Lipinski	Synthetic accessibility	LD_{50} (mg/kg)	Predicted toxicity class
Naringin	$C_{27}H_{32}O_{14}$	580.53	225.06	–0.87	–2.98	Low	No; 3 violations: MW>500, NorO>10, NHorOH>5	6.16	2300	5
Formononetin	$C_{16}H_{12}O_4$	268.26	59.67	2.66	–3.73	High	Yes	2.81	2500	5
Coumestrol	$C_{15}H_8O_5$	268.22	83.81	2.46	–3.87	High	Yes	3.16	2991	4
Quercetin	$C_{15}H_{10}O_7$	131.36	1.23	1.23	–3.16	High	Yes	3.23	159	3
Galangin	$C_{15}H_{10}O_5$	270.24	90.90	1.99	–3.46	High	Yes	3.12	3919	5
Naringenin	$C_{15}H_{12}O_5$	272.25	86.99	1.84	–3.49	High	Yes	3.01	2000	4
Chrysin	$C_{15}H_{10}O_4$	70.67	70.67	2.55	–4.19	High	Yes	2.93	3919	5
Hesperetin	$C_{16}H_{14}O_6$	302.28	96.22	1.91	–3.62	High	Yes	3.22	2000	4
Genistein	$C_{15}H_{10}O_5$	270.24	90.90	2.04	–3.72	High	Yes	2.87	2500	5
Chlorogenic acid	$C_{16}H_{18}O_9$	354.31	164.75	-0.39	–1.62	Low	Yes; 1 violation: NHorOH>5	4.16	5000	5
Ferulic acid	$C_{10}H_{10}O_4$	194.18	66.76	1.36	–2.11	High	Yes	1.93	1772	4
Caffeic acid	$C_9H_8O_4$	180.16	77.76	0.93	–1.89	High	Yes	1.81	2980	5
10-Hydroxy-2-decenoic acid	$C_{10}H_{18}O_3$	186.25	57.53	1.95	–1.83	High	Yes	2.41	3000	5

3.4. Molecular docking.

To validate the molecular docking method used in this study, we first calculated the RMSD by redocking AP23451 into the Src kinase protein's original pocket (PDB). This procedure was completed using several approaches and grid box size searches, as presented in Table 3. Based on the results, we found that with the grid box size set, the RMSD value showing < 2 Å was obtained at a size of 5 Å, with an RMSD value of 1.3685 Å. Figure 4 illustrates the visualization of the 5 Å grid box, where AP23451 was observed to return to its original position, with an RMSD value smaller than that of the other sizes. Through the procedure we applied, this grid box size met the criteria for determining the optimal grid box size. Therefore, for the molecular docking, we used a 5 Å grid box size.

Table 3. Grid box size search based on RMSD values.

Grid box (Å)	RMSD (Å)
1	1.4783
2.5	1.5316
5	1.3685
7.5	1.468
10	1.5093

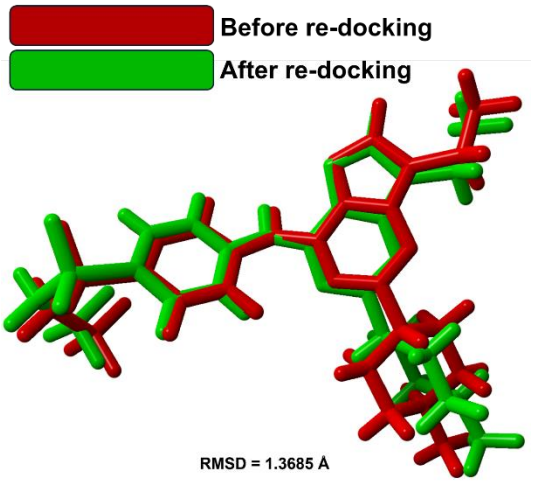

Figure 4. Re-docking AP23451 into its initial position. Red color initial position. Green color re-docking position.

In this study, molecular docking was performed using the VINA algorithm with QM-AM1 applied to assist in the calculations. The Src kinase protein, as the target, was set to a rigid condition, and the 5 Å grid box was applied. We then ran the docking of the ligand into the 5 Å grid box area. Based on the results, the test compounds from royal jelly had binding energies ranging from 5.512 to 9.08 kcal/mol. AP23451, as the control inhibitor, had the highest binding energy value in this study. The test compound with a binding energy closest to that of AP23451 was naringin, with a binding energy of 9.08 kcal/mol, followed by formononetin with a binding energy of 8.243 kcal/mol. Surprisingly, we also found that SCHEMBL7608488, as the control reference, had a lower binding energy value of 7.771 kcal/mol (Table 4). Therefore, we selected the test compound with the highest binding energy. However, based on previous ADMET predictions indicating that naringin exhibited less favorable characteristics, we decided to proceed with formononetin as the potential test compound for further analysis. Additionally, AP23451, as the control inhibitor, was used for comparison in interaction analysis and molecular dynamics simulations.

Table 4. Binding energy of test compounds against the Src kinase protein.

Rank	CID	Compound	Binding energy (kcal/mol)
1	-	AP23451 (Control inhibitor)	10.468
2	442428	Naringin	9.08
3	5280378	Formononetin	8.243
4	5281707	Coumestrol	8.041
5	5280343.	Quercetin	7.995
6	5281616	Galangin	7.924
7	439246	Naringenin	7.917
8	5281607	Chrysin	7.915
9	72281	Hesperetin	7.838
10	70144047	SCHEMBL7608488 (Control reference)	7.771
11	5280961	Genistein	7.743
12	1794427	Chlorogenic acid	7.526
13	445858	Ferulic acid	6.347
14	689043	Caffeic acid	6.269
15	5312738	10-Hydroxy-2-decenoic acid	5.512

3.5. Post-docking analysis.

Table 5 presents the data from the analysis of complex interactions between selected protein-ligand complexes, specifically the Src Kinase-Formononetin complex and the Src Kinase-AP23451 complex. AP23451, serving as the control inhibitor with the highest binding energy, is characterized by hydrogen bonding in the form of conventional hydrogen bonds and hydrophobic interactions such as Pi-alkyl and alkyl types. The conventional hydrogen bonds in the Src Kinase-AP23451 complex occur from Met341 (H-donor) to UNK14 (H-acceptor), from Lys343 (H-donor) to UNK14, and from UNK15 (H-donor) to Met341 (H-acceptor). We found that Met341 is located in pocket 1 and pocket 2, which are potential binding sites for Src kinase. We suggest that one of the main reasons AP23451 interacts effectively with Src kinase is hydrogen bonding within these potential binding-site pockets, with distances of 1.97399, 2.18093, and 2.46137 Å. Meanwhile, the hydrophobic interactions range from 3.61122 to 5.20784 Å. We also observed attractive electrostatic interactions, such as salt bridges, resulting from positive chemistry interacting with negative chemistry. This complex primarily exhibits hydrogen bonds, totaling 3 (Figure 5A).

Table 5. Interactions of selected test compounds and the control inhibitor with the Src kinase protein.

Complex enzyme-ligand	Name	Distance (Å)	Category	Types	From	From chemistry	To	To chemistry
Src kinase-AP23451	A:ARG291: HH21 - A:UNK15: O	2,30869	Hydrogen bond; electrostatic	Salt bridge; attractive charge	A: ARG291: HH21	H-donor; positive	A: UNK15: O	H-acceptor; negative
	A:LYS343: NZ - A:UNK15: O	5,49244	Electrostatic	Attractive charge	A: LYS343: NZ	Positive	A: UNK15: O	Negative
	A:LYS343: NZ - A:UNK15: O	3,2998	Electrostatic	Attractive charge	A: LYS343: NZ	Positive	A: UNK15: O	Negative
	A:LYS343: NZ - A:UNK15: O	5,00819	Electrostatic	Attractive charge	A: LYS343: NZ	Positive	A: UNK15: O	Negative
	A:MET341: H - A:UNK15: N	2,46137	Hydrogen bond	Conventional hydrogen bond	A:MET341 : H	H-donor	A: UNK15: N	H-acceptor

Complex enzyme-ligand	Name	Distance (Å)	Category	Types	From	From chemistry	To	To chemistry
	A:LYS343:HZ3 - A:UNK15:O	2,18093	Hydrogen bond	Conventional hydrogen bond	A:LYS343:HZ3	H-Donor	A: UNK15:O	H-acceptor
	A:UNK15:H - A:MET341:O	1,97399	Hydrogen bond	Conventional hydrogen bond	A: UNK15:H	H-Donor	A: MET341:O	H-acceptor
	A:VAL281 - A:UNK15	4,79667	Hydrophobic	Alkyl	A:VAL281	Alkyl	A: UNK15	Alkyl
	A:ALA293 - A:UNK15:C	4,46669	Hydrophobic	Alkyl	A:ALA293	Alkyl	A: UNK15:C	Alkyl
	A:UNK15:C - A:LYS295	4,90924	Hydrophobic	Alkyl	A: UNK15:C	Alkyl	A: LYS295	Alkyl
	A:UNK15:C - A:VAL323	4,51161	Hydrophobic	Alkyl	A: UNK15:C	Alkyl	A: VAL323	Alkyl
	A:UNK15:C - A:LEU393	5,00865	Hydrophobic	Alkyl	A:UNK15:C	Alkyl	A: LEU393	Alkyl
	A:UNK15 - A:LEU273	5,22266	Hydrophobic	Alkyl	A: UNK15	Alkyl	A: LEU273	Alkyl
	A:UNK15 - A:ALA293	3,61122	Hydrophobic	Pi-Alkyl	A: UNK15	Pi-Orbitals	A: ALA293	Alkyl
	A:UNK15 - A:LEU393	4,64449	Hydrophobic	Pi-Alkyl	A: UNK15	Pi-Orbitals	A: LEU393	Alkyl
	A:UNK15 - A:LEU273	4,51077	Hydrophobic	Pi-Alkyl	A: UNK15	Pi-Orbitals	A: LEU273	Alkyl
	A:UNK15 - A:VAL281	5,20784	Hydrophobic	Pi-Alkyl	A: UNK15	Pi-Orbitals	A: VAL281	Alkyl
	A:UNK15 - A:ALA293	5,1235	Hydrophobic	Pi-Alkyl	A: UNK15	Pi-Orbitals	A: ALA293	Alkyl
	A:UNK15 - A:LEU393	4,94666	Hydrophobic	Pi-Alkyl	A: UNK15	Pi-Orbitals	A: LEU393	Alkyl
	A:UNK15 - A:LEU273	4,89236	Hydrophobic	Pi-Alkyl	A: UNK15	Pi-Orbitals	A: LEU273	Alkyl
Src kinase-formononetin	A:MET341:H - A:UNK6:O	2,5054	Hydrogen bond	Conventional hydrogen bond	A:MET341:H	H-Donor	A: UNK6: O	H-acceptor
	A:TYR340:HA - A:UNK6:O	2,85586	Hydrogen bond	Carbon-hydrogen bond	A:TYR340:HA	H-Donor	A: UNK6: O	H-acceptor
	A:GLY344:HA1 - A:UNK6:O	2,49183	Hydrogen Bond	Carbon-hydrogen bond	A:GLY344:HA1	H-Donor	A: UNK6: O	H-acceptor
	A:UNK6:H3 - A:ASP404:OD1	2,88723	Hydrogen bond	Carbon-hydrogen bond	A: UNK6:H3	H-Donor	A: ASP404:OD1	H-acceptor
	A:ALA403 - A:UNK6:C	3,86548	Hydrophobic	Alkyl	A:ALA403	Alkyl	A: UNK6: C	Alkyl
	A:UNK6:C - A:LYS295	4,7943	Hydrophobic	Alkyl	A:UNK6:C	Alkyl	A: LYS295	Alkyl
	A:UNK6:C - A:VAL323	3,8372	Hydrophobic	Alkyl	A: UNK6:C	Alkyl	A: VAL323	Alkyl
	A:UNK6 - A:LEU273	4,26413	Hydrophobic	Pi-alkyl	A: UNK6	Pi-orbitals	A: LEU273	Alkyl
	A:UNK6 - A:ALA293	5,08013	Hydrophobic	Pi-alkyl	A: UNK6	Pi-orbitals	A: ALA293	Alkyl
	A:UNK6 - A:LEU273	4,41839	Hydrophobic	Pi-alkyl	A: UNK6	Pi-orbitals	A: LEU273	Alkyl

Complex enzyme-ligand	Name	Distance (Å)	Category	Types	From	From chemistry	To	To chemistry
	A:UNK6 - A:ALA293	3,51916	Hydrophobic	Pi-alkyl	A: UNK6	Pi-orbitals	A: ALA293	Alkyl
	A:UNK6 - A:LEU393	4,59075	Hydrophobic	Pi-alkyl	A: UNK6	Pi-orbitals	A: LEU393	Alkyl

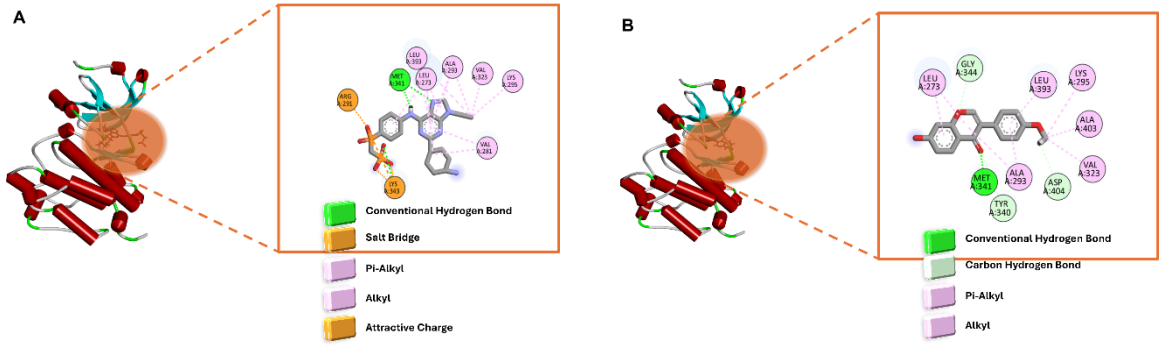

Figure 5. 2D and 3D visualizations of Src kinase-ligand complex interactions. **(a)** Src kinase-AP23451 complex; **(b)** Src kinase-formononetin complex.

For the Src kinase-formononetin complex (Figure 5B), we observed characteristics similar to those seen in the Src Kinase-AP23451 complex, including hydrogen bonding between the ligand and the Met341 amino acid residue. The bond length for this hydrogen bond is 2.5054 Å. Formononetin also binds to Tyr340 through a carbon-hydrogen bond with a distance of 2.85586 Å. The carbon-hydrogen bond type predominates in this complex, occurring in two additional amino acid residues: Gly344 and Asp404. Hydrophobic interactions in this study have bond distances ranging from 3.51916 Å to 5.08013 Å. Notably, the Src kinase-formononetin complex features four hydrogen bonds, more than in the Src Kinase-AP23451 complex. Therefore, based on the more dominant hydrogen bond characteristics resulting from the interaction of the test compound formononetin with Src kinase, formononetin is considered a promising inhibitor of Src kinase.

We performed molecular docking to understand how test compounds from royal jelly interact with the Src kinase target and to evaluate their binding affinity using binding energy. Molecular docking has been widely used to identify potential inhibitor candidates. In a cancer study by Mendie and Hemalatha [61], molecular docking was used to suggest inhibitor candidates targeting growth factor receptors (GFRs), which were inhibited using phytochemicals. In this study, we evaluated the highest binding energy, and AP23451, as a control inhibitor, showed a higher value than the test compounds from royal jelly, followed by naringin. However, based on the ADMET property prediction, which was less favorable, we did not consider naringin for further analysis and instead chose formononetin for further investigation.

In the Src kinase-AP23451 complex, we found that hydrogen bonding was less frequent compared to the Src kinase-formononetin complex. We considered the type of hydrogen bonding because it enhances stability within the protein-ligand complex. Additionally, hydrophobic interactions formed contribute to the test compound's mechanism of action and guide further optimization [62,63]. Moreover, several studies have shown that hydrogen bonds are the strongest interactions formed between the ligand's OH group and amino acids on the target protein, leading to higher binding efficiency [64]. Formononetin, which anchors to the active sites Met341 and Gly344 in pockets 1 and 2 through hydrogen bonds, ensures good

stability, as indicated by favorable hydrogen bond distances of 2.5054 and 2.49183 Å. A hydrogen bond distance below 2.5 Å is typically considered optimal [65].

3.6. QSAR analysis.

The quantitative structure-activity relationship (QSAR) analysis in this study was conducted using the free PASS online server, which predicts and evaluates the potential anticancer activity of selected compounds, formononetin, with AP23451 as a comparator. QSAR assists us by utilizing chemical structure data in SMILES format to understand the biological functions of these compounds. Based on the evaluation results presented in Table 6, the prediction indicates that formononetin is significantly more potent as an anticancer agent than AP23451. This is evidenced by the fact that the Pa value is greater than Pi, suggesting formononetin's potential as a versatile antineoplastic agent. Validation and confirmation through QSAR analysis, based on the post-docking findings, show a positive correlation.

Table 6. Pa and Pi values from PASS online for QSAR analysis.

Anticancer	**Compound**			
	AP23451		**formononetin**	
	Pa	**Pi**	**Pa**	**Pi**
Breast cancer-resistant protein inhibitor	-	-	0,805	0,001
Antineoplastic (breast cancer)	-	-	0,526	0,016
Antineoplastic (uterine cancer)	-	-	0,480	0,004
Prostate cancer treatment	-	-	0,395	0,023
Antineoplastic (cervical cancer)	-	-	0,322	0,016
Antineoplastic (small cell lung cancer)	-	-	0,291	0,036
Antineoplastic (bone cancer)	0,406	0,003	0,264	0,019
Antineoplastic (colorectal cancer)	-	-	0,257	0,046
Antineoplastic (colon cancer)	-	-	0,248	0,043
Antineoplastic (lung cancer)	-	-	0,205	0,068
Antineoplastic (brain cancer)	-	-	0,219	0,095
Antineoplastic (gastric cancer)	-	-	0,153	0,051
Antineoplastic (ovarian cancer)	-	-	0,130	0,076
Antineoplastic (renal cancer)	-	-	0,149	0,117

3.7. DFT analysis.

To investigate the molecular structure and properties of the test compound formononetin, density functional theory calculations were performed using quantum mechanical methods. DFT employs electron density functions, which can show the energy of a molecule. Figure 6A illustrates the control inhibitor AP23451 and the formononetin compound (an isoflavonoid) shown in Figure 6B, both of which have been geometry-optimized using the ORCA software. Calculations were then applied to determine the HOMO (highest occupied molecular orbital) and LUMO (lowest unoccupied molecular orbital) energies. The results indicate that formononetin has a HOMO energy of –0.2075 eV and a LUMO energy of –0.0537 eV. The HOMO energy suggests that formononetin has the ability to donate electrons, acting as a Lewis base. In Figure 7B, the spatial distribution of electrons in the HOMO is shown, with areas of the compound structure exhibiting the highest electron density marked in darker colors. The HOMO electron density is mainly concentrated around the aromatic ring of formononetin. The LUMO energy, being lower, indicates a relatively stable orbital that can effectively accept electrons. In Figure 7B, the transparent green areas show the LUMO distribution, with electron density concentrated around the hydroxyl (–OH) substituent on the benzene ring.

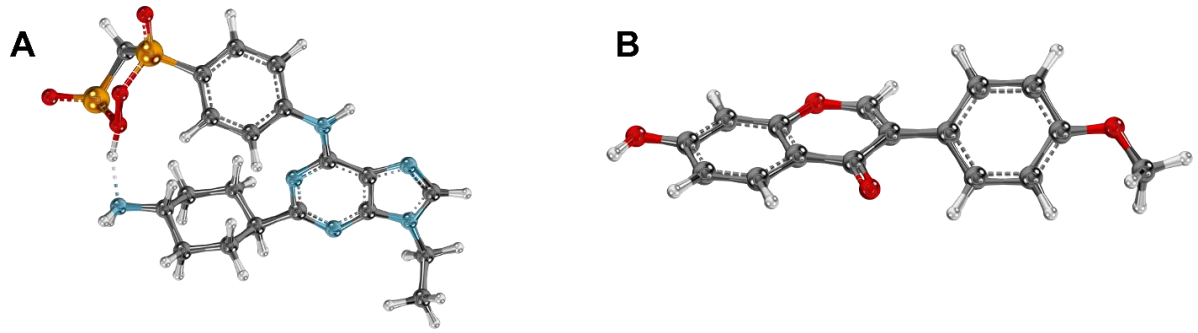

Figure 6. Optimization of the compound **(a)** AP23451; **(b)** Formononetin.

From the HOMO and LUMO energy levels, the energy gap was calculated, yielding a value of −0.15380 eV for formononetin (Figure 7A) and −0.17450 eV for AP23451 (Figure 7B). This value indicates that formononetin is predicted to be stable. We also calculated the molecular properties based on the HOMO and LUMO energies for both formononetin and the control inhibitor AP23451, as presented in Table 7. Formononetin has an ionization potential of 0.20750 eV, which indicates the weakest energy required to remove an electron from the molecule. The calculated electron affinity yielded a value of 0.05370 eV. The chemical potential of formononetin is –0.13060 eV, providing insight into the tendency of the species to act or shift. The calculated electronegativity value is 0.13060 eV, offering a prediction of the charge distribution. The values for hardness and softness were 0.07690 eV and 6.50195 eV, respectively. Hardness reflects a system's resistance to polarization, while softness indicates its susceptibility to changes in polarization. Finally, the electrophilicity index for formononetin was 0.11090 eV, indicating its ability to accept electrons.

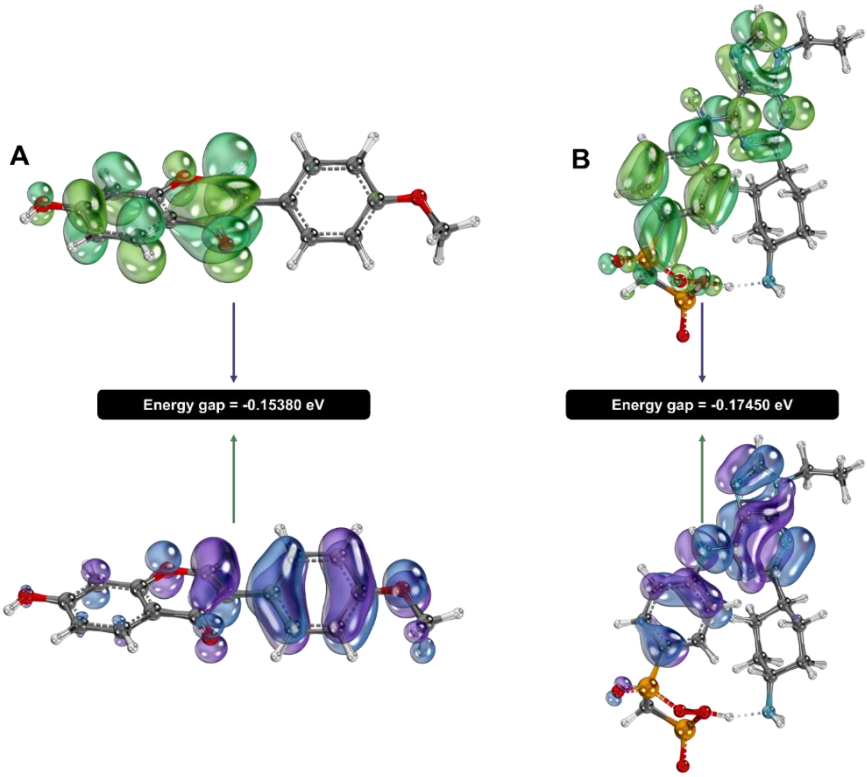

Figure 7. Frontier molecular orbitals (HOMO and LUMO). **(a)** FMO calculations (HOMO and LUMO) and energy gap for the test compound formononetin; **(b)** FMO calculations (HOMO and LUMO) and energy gap for the control inhibitor AP23451.

Table 7. Molecular properties of formononetin and AP23451.

Properties	Formononetin	AP23451
Energy HOMO (eV)	–0.2075	–0.2244
Energy LUMO (eV)	–0.0537	–0.0499
Energy gap	–0.15380	–0.17450
Ionization potential (I) (eV)	0.20750	0.22440
Electron affinity (A) (eV)	0.05370	0.04990
Chemical potentials (μ) (eV)	–0.13060	–0.13715
Electronegativity (χ) (eV)	0.13060	0.13715
Hardness (η) (eV)	0.07690	0.08725
Softness (S) (eV)	6.50195	5.73066
Electrophilicity index (ω) (eV)	0.11090	0.10779

From the overall DFT calculations, we highlight the energy gap results for both AP23451 and formononetin. AP23451 has an energy gap of –0.17450 eV, while formononetin has an energy gap of –0.15380 eV. The energy gap provides an indication of the stability and reactivity of a molecule. A higher energy gap is generally correlated with better stability and lower reactivity. Therefore, based on DFT calculations and observations of the frontier molecular orbitals (FMOs) and molecular properties, we predict that formononetin is stable and less reactive than the control inhibitor AP23451, making it a promising candidate for inhibition.

We applied quantum mechanics (QM), which helps us account for all energy contributions. On the other hand, QM-based performance has general properties across chemical space, making it possible to consider all elements and interactions on a unified basis [66]. Our observations of the test compound formononetin through DFT calculations provided insights into the FMO. These FMO, consisting of the HOMO and the LUMO, provide insights into the compound's kinetic stability and chemical reactivity [67]. DFT helps study charge distribution and molecular behavior. The energies of HOMO and LUMO provide insights into quantum mechanical parameters that influence chemical interactions. DFT calculations aim to complement docking studies and molecular dynamics simulations [68]. Finally, DFT has facilitated the evaluation of reactivity and stability in potential candidates [69].

3.8. Post-MD analysis.

At this stage, we performed molecular dynamics (MD) simulations to assess the stability, fluctuations, energy distribution, and binding energy calculations for the Src kinase-Formononetin complex. To evaluate the quality of this complex, we ran the Src kinase-AP23451 complex as a comparison, as well as the Src kinase protein in the absence of the inhibitor (apoform). Based on the results, our analysis revealed changes in the interactions within the Src kinase-ligand complex, as shown in Figure 8. AP23451 released its electrostatic bonds with Arg291 and Lys343. However, this type of bond persisted even after 200 ns, specifically binding to the amino acid residue Asp348. Hydrogen bonding, as the dominant interaction, was observed, with AP23451 visually showing both maintained and newly formed hydrogen bonds. The maintained hydrogen bonds interact with Met341, while the newly formed hydrogen bonds in the Src kinase-AP23451 complex interact with Glu399 and Gln275 (Figure 8A). Interestingly, formononetin released its hydrogen bonds after 200 ns in the MD simulation and formed hydrophobic interactions instead. We predict that these hydrophobic interactions contribute to the stability of the Src kinase-formononetin complex (Figure 8B). This conclusion is supported and further confirmed by the root mean square deviation (RMSD) values obtained for both compounds before (0 ns) and after (200 ns) MD simulation. As

visualized and presented in Figure 9, the position of AP23451 returned to the Src kinase protein pocket area, but with an RMSD value of 2.1395 Å (Figure 9A). In contrast, formononetin shifted back into the Src kinase protein pocket with minimal displacement, as evidenced by an RMSD value of 0.9945 Å (Figure 9B). In this context, the RMSD value indicates that, while the ligand undergoes conformational fluctuations, the graph in Figure 9 shows that formononetin remains more stable than AP23451. This stability is correlated with both the graphical production and RMSD values.

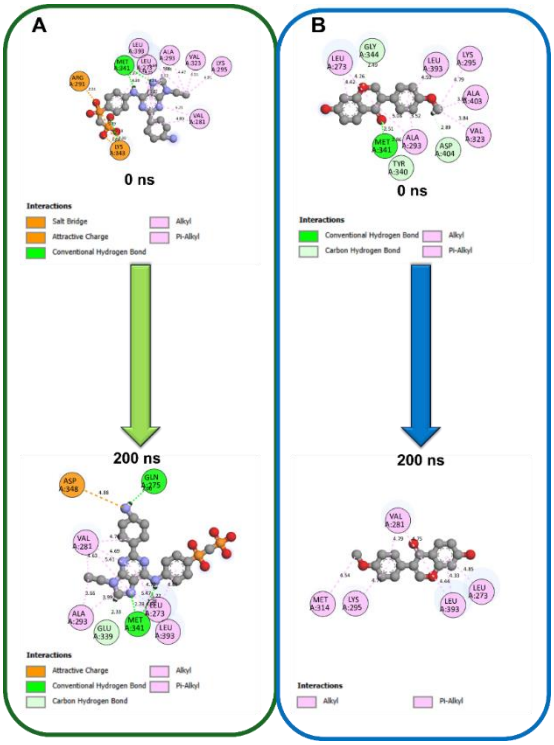

Figure 8. Changes in interactions within the Src kinase-ligand complex. **(a)** AP23451; **(b)** formononetin.

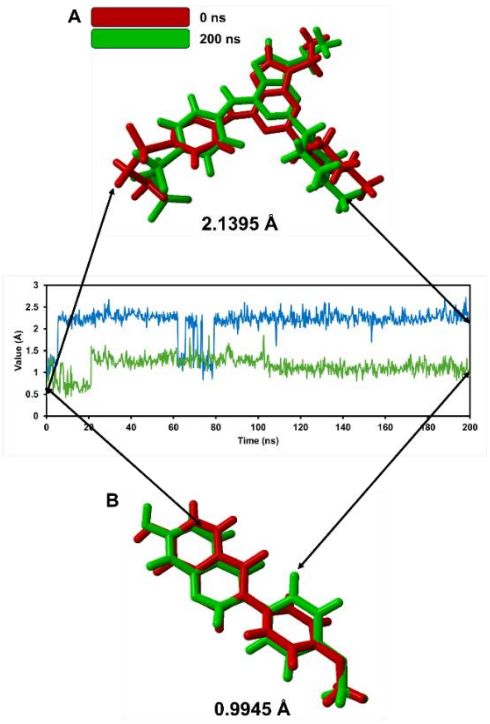

Figure 9. Ligand conformation during the 200 ns MD simulation trajectory. **(a)** AP23451; **(b)** Formononetin.

After examining the insights from the compound movements, we evaluated the post-MD results using several parameters to observe the changes occurring in the protein-ligand complex. Figure 10A shows the evaluation based on RMSD of Calpha (RMSDCa), where we observe the apoprotein, the Src kinase-AP23451 complex, and the Src kinase-formononetin complex. In the RMSDCa production, AP23451 had a significant effect on the RMSDCa value from the start at 0 ns to 11.25 ns, reaching a value of 3.191 Å. In the case of the apoprotein, at the 11.25 ns trajectory, the RMSDCa production was only 2.393 Å. Formononetin showed a low RMSDCa value of 2.294 Å at the 11.25 ns mark for the Src kinase protein. After 11.25 ns, the Src kinase-AP23451 complex exhibited relatively higher RMSDCa production compared to both the apoprotein and the formononetin complex, as seen in the RMSDCa production graph in Figure 10A. The data indicate that the Src kinase-formononetin complex produced a consistently lower average RMSDCa value compared to both the apoprotein and the Src kinase-AP23451 complex, with average values of 2.236, 2.791, and 2.136 Å, respectively.

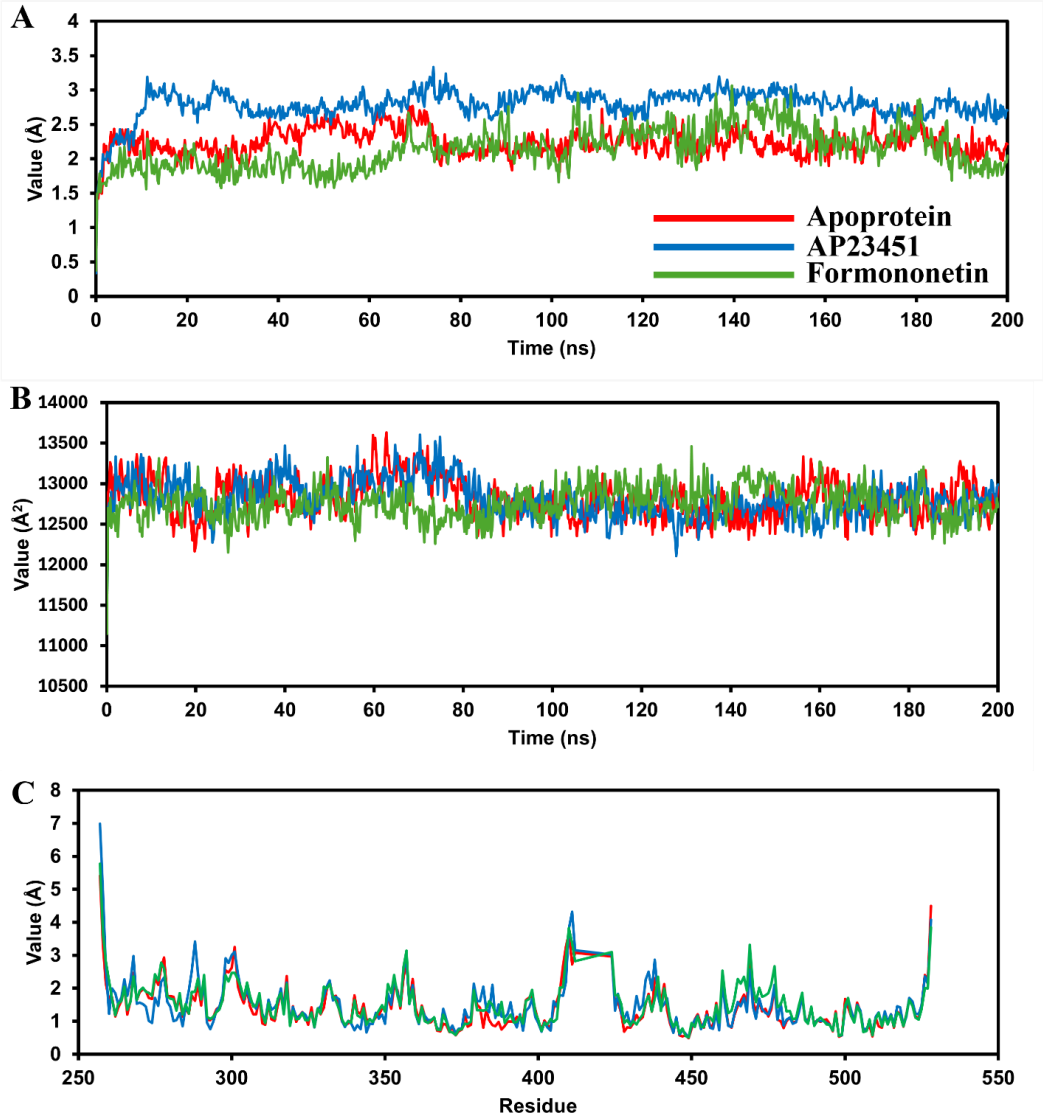

Figure 10. 200 ns MD simulation of the apoprotein, Src kinase-AP23451 complex, and Src kinase-formononetin complex. **(a)** RMSD Calpha; **(b)** SASA; **(c)** RMSF.

To understand the changes and shrinkage of the Src kinase protein upon ligand binding in the Src kinase pocket, we evaluated the complex using SASA, as shown in Figure 10B. In surface area changes, the apoprotein, which does not have any ligand interacting with the Src

kinase protein, showed an opening in the area at the 62.75 ns trajectory with a value of 13630.637 Å² (the highest SASA value in the apoprotein). At the same 62.75 ns trajectory, our investigation found that the Src kinase-AP23451 complex and the Src kinase-Formononetin complex had values of 13131.232 and 12659.494 Å², respectively. Both values were lower compared to the apoprotein (as observed at the 62.75 ns trajectory). The presence of interactions with both compounds demonstrates that the Src kinase protein undergoes contraction. This was also confirmed by the average SASA values for the apoprotein and both complexes. Our calculations showed that the Src kinase-formononetin complex had the lowest average value, 12758.677 Å², while the Src kinase-AP23451 complex had an average value of 12814.377 Å².

To evaluate fluctuations at the amino acid level in the Src kinase protein due to ligand binding or its absence (apoprotein), we assessed RMSF (Figure 10C). The apoprotein had an average RMSF value of 1.414 Å. This was the lowest value since none of the amino acid residues in the Src kinase protein interacted with the compound. When the Src kinase protein interacted with AP23451 throughout the 200 ns trajectory, the average RMSF value was 1.467 Å. In contrast, when formononetin interacted with the Src kinase protein, it caused a fluctuation with an average RMSF value of 1.487 Å. We specifically observed Met341 and found that AP23451 interacted with It with a low fluctuation of 0.885 Å, whereas formononetin interacted with It, showing a fluctuation of 1.175 Å. The apoprotein, on the other hand, showed that Met341 had a value of 1.291 Å when it was not interacting with any compound. Thus, the compound-induced low fluctuation suggests that the interaction between the compound and Src kinase is more stable.

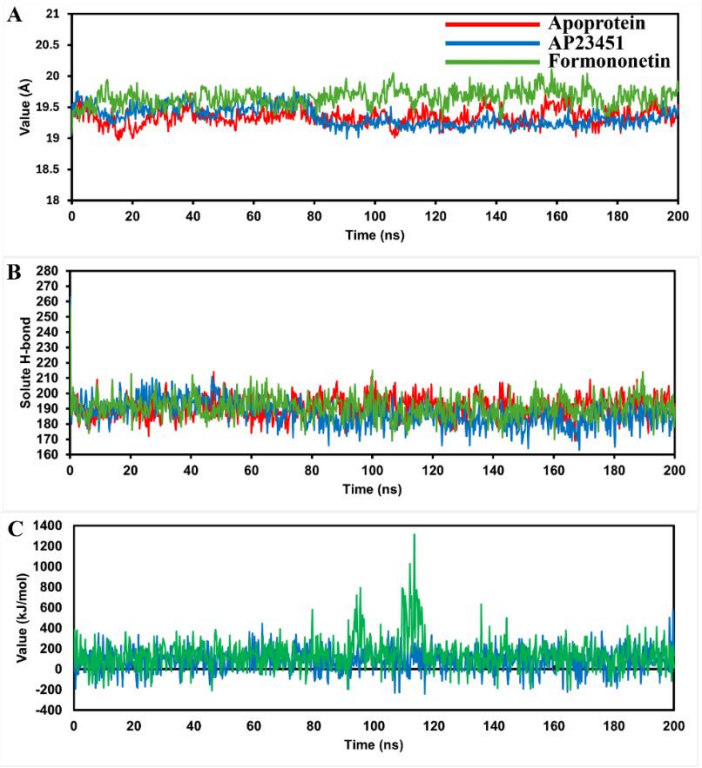

Figure 11. 200 ns MD simulation on apoprotein, Src kinase-AP23451 complex, and Src kinase-formononetin complex. **(a)** Rg; **(b)** H-bond; **(c)** Binding energy.

To measure and provide insights into the structural density of Src kinase, we evaluated it using the radius of gyration (Rg). When the Src protein tends to adopt a more compact structure, the stability of the protein can be achieved in the MD simulation. Based on our

calculations, we observed the Rg values and presented the results in Figure 11A. We found that the apoprotein tends to produce the lowest value, 18.964 Å, while the Src kinase-AP23451 complex shows the lowest value of 18.994 Å at the 90.75 ns trajectory. In this Rg evaluation, the Src kinase-Formononetin complex has an average value of 19.653 Å. Figure 11B shows the hydrogen bond production graph over the 200 ns trajectory. The apoprotein has an average value of 190.638 Å, the Src kinase-AP23451 complex has an average value of 187.016 Å, and the Src kinase-Formononetin complex has an average value of 191.034 Å.

To evaluate the binding energy of the protein-ligand complex, we calculated it using the MM-PBSA method. The MM-PBSA method was applied to both the Src kinase-AP23451 and Src kinase-Formononetin complexes. The results show that AP23451 has a binding energy value of only 84.802 kJ/mol, while formononetin has a binding energy of 143.532 kJ/mol with the Src kinase protein. Formononetin interacts with the Src kinase protein much more effectively than AP23451—the more positive the binding energy value, the stronger the bond. As presented in Figure 11C, the binding energy production graph tends to show positive values. We infer greater stability from the binding energy evaluation using the MM-PBSA method. In the context of anticancer studies, the MM-PBSA method is a widely used, endpoint-free energy calculation method for determining ligand binding affinity. MM-PBSA offers significant advantages by enabling the identification of high-activity regions, evaluation of binding affinity, and prediction of structural stability. Ultimately, the MM-PBSA method is considered effective for identifying inhibitors of target proteins (target receptors) in the drug discovery pipeline. Furthermore, the resulting data can be integrated with experimental data, thereby enhancing confidence and validation [70,71].

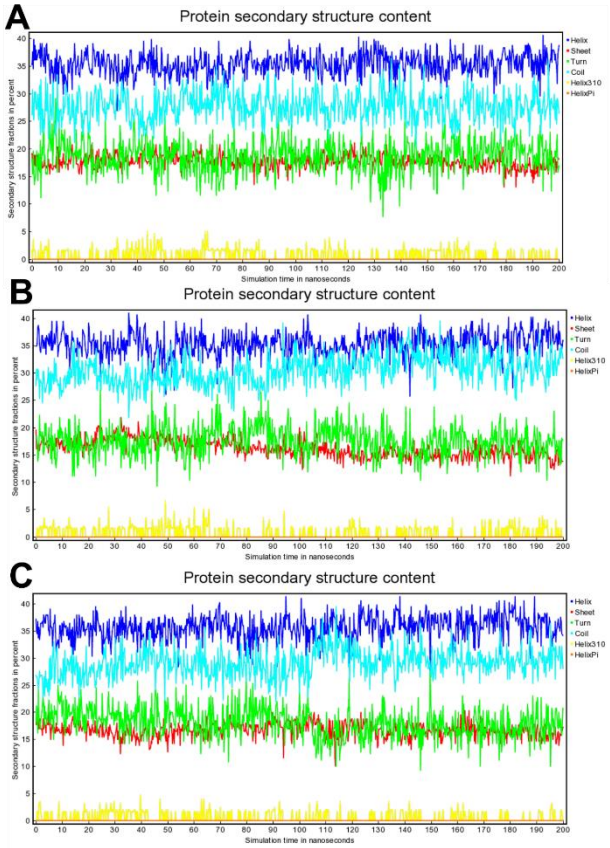

Figure 12. Protein secondary structure content. **(a)** Apoprotein; **(b)** Src kinase-AP23451 complex; **(c)** Src kinase-formononetin complex.

Figure 12A presents the graph of the apoprotein's secondary structure content. The evaluation performed during the 200 ns trajectory simulation includes helix, sheet, turn, coil, helix310, and helixPi in the Src kinase protein. The protein folding of the Src kinase-AP23451 complex is shown in Figure 12B, while the Src kinase-Formononetin complex is presented in Figure 12C.

In the MD simulation study, our investigation showed that stability was achieved in the Src kinase-formononetin complex. This indication was derived from a series of post-MD evaluations of the large data set generated during the 200 ns simulation trajectory. Evaluations using RMSDCa, SASA, RMSF, Rg, H-bond, and binding energy were key components in understanding the movement of the protein-ligand complex over time. The MM-PBSA method we applied helped calculate binding energy, as this method is particularly useful in scoring systems to assess the binding affinity between a ligand and its target protein [70-73]. This study shows that formononetin exhibits a higher binding energy than the control inhibitor, indicating its strong potential as an anticancer candidate targeting Src kinase. This study has explored detailed information regarding receptor-ligand interactions. A receptor is a target utilized and serves as the focus in the process of healing and preventing a disease. In a biological context, the interaction between a ligand and its target receptor can be evaluated by calculating binding affinity and identifying the most potent therapeutic molecular orientation through binding pocket analysis obtained from docking studies. Additionally, molecular dynamics (MD) simulations can investigate biomolecular interactions during biological processes and elucidate the mechanisms that accompany them[72,73].

Previous computational studies on Src kinase have demonstrated the value of combining docking, DFT, and molecular dynamics simulations for identifying novel inhibitors, thereby providing a framework for benchmarking the present work. For example, Khamouli *et al*. [24] employed ligand-based pharmacophore modeling, 3D-QSAR, docking, DFT calculations, and MD simulations to identify CID_70144047 as a promising c-Src inhibitor, emphasizing the importance of integrating multi-level computational analyses in Src-targeted drug discovery. Similarly, Rolta *et al*. [74] used docking and long-timescale MD simulations to screen phytoconstituents against Src kinase and identified apigenin as a stable, drug-like inhibitor with interactions comparable to those of bosutinib. Compared with these studies, our results show that the bioactive compounds from RJ, particularly formononetin, exhibit binding stability and interaction patterns that are consistent with the profiles of previously reported Src inhibitors, while also offering a distinct natural-product-based chemical space that has not been explored in earlier Src-focused computational research. This comparison underscores that our integrated docking–DFT–MD approach aligns with established computational strategies while expanding the potential Src inhibitor landscape through a novel nutraceutical source.

3.9. PCA, RMSD Histogram, and DCCM analysis.

The values generated from our MD simulations were analyzed using principal component analysis (PCA). PCA helped us understand the stability of the conformations and the thermodynamics of the system. It allowed us to reduce the complexity of the data and identify the main patterns within the analyzed dataset. Based on the analysis, the apoprotein, which does not bind any compounds, showed PC1, PC2, and PC3 values of 22.01%, 11.03%, and 8.06%, respectively (Figure 13A). The graph shows the proportion of variance, with the peak value at 22%. When the Src kinase protein interacts with AP23451, we observed an increase in PC1 to 26.68% and PC2 to 11.08%, but a decrease in PC3 to 6.85% (Figure 13B).

For the Src kinase-formononetin complex, we found that the values for PC1 and PC2 were higher compared to the Src kinase-AP23451 complex (Figure 13C). A comparison of the two complexes with the apoprotein is shown visually in Figure 13. If the clusters overlap (indicated by the red and blue colors), it suggests a similarity in the distribution of internal energy. A high density at low RMSD values indicates the stability of the Src kinase protein and suggests minimal conformational changes.

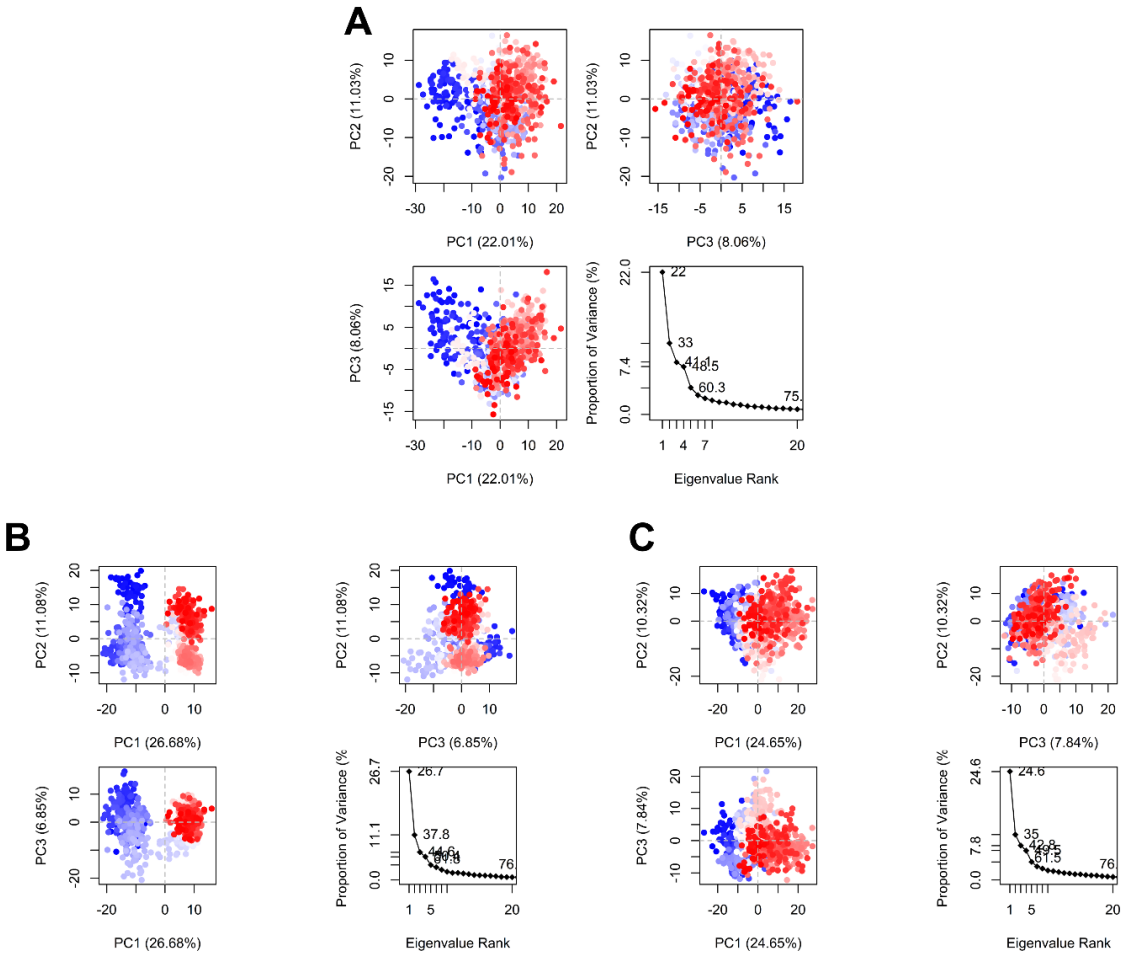

Figure 13. Principal component analysis based on the 200 ns MD simulation trajectory. **(a)** Apoprotein; **(b)** Src kinase-AP23451 complex; **(c)** Src kinase-formononetin complex.

To visualize the frequency distributions of values in the 200 ns trajectories for the apoprotein, the Src kinase-AP23451 complex, and the Src kinase-formononetin complex, we used the RMSD histogram. Figure 14A shows that the apoprotein's RMSD histogram has a red peak at RMSD values lower than 2.5, whereas the Src kinase-AP23451 complex tends to have a peak at values above 2.5 (Figure 14B). The RMSD histogram for the Src kinase-formononetin complex tends to follow the pattern of the apoprotein, particularly when considering the peak of the graph (Figure 14C). The distribution at specific peaks reflects the balance and stability of the conformations.

Figure 15 shows the dynamics cross-correlation matrix (DCCM) plot, which provides insight into the positive correlation and anticorrelation in the protein's conformation. If the DCCM plot predominantly shows red colors, it indicates that the conformation is becoming more stable, with minimal structural disturbances. The DCCM plot correlates with the RMSDCa. Figure 15A presents the DCCM plot for the apoprotein, which shows a predominance of red. In contrast, the DCCM plot for the Src kinase-AP23451 complex (Figure 15B) is different. The DCCM plot for the Src kinase-formononetin complex (Figure 15C)

exhibits characteristics closer to the apoprotein, with a color pattern that is more similar. The stability of the Src kinase-formononetin complex is confirmed to be stable, as seen in the RMSDCa analysis.

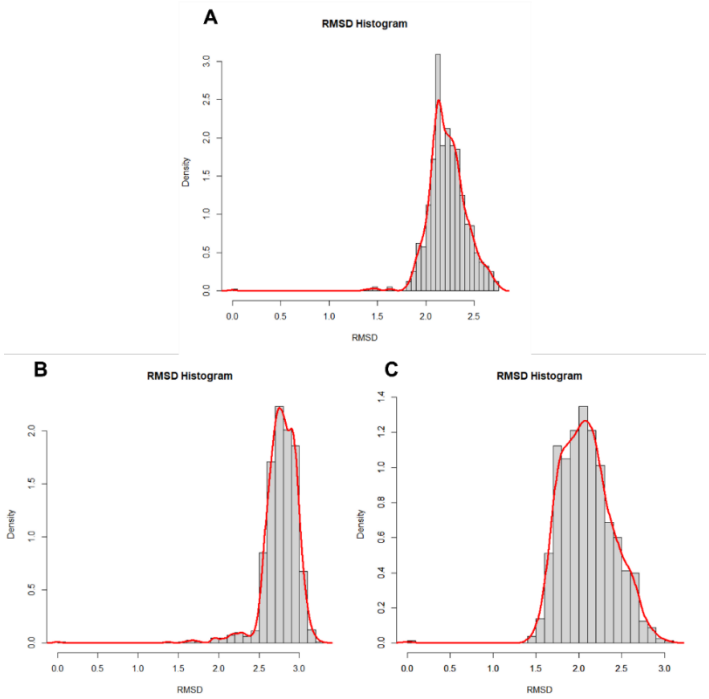

Figure 14. RMSD Histogram. **(a)** Apoprotein; **(b)** Src kinase-AP23451 complex; **(c)** Src kinase-formononetin complex.

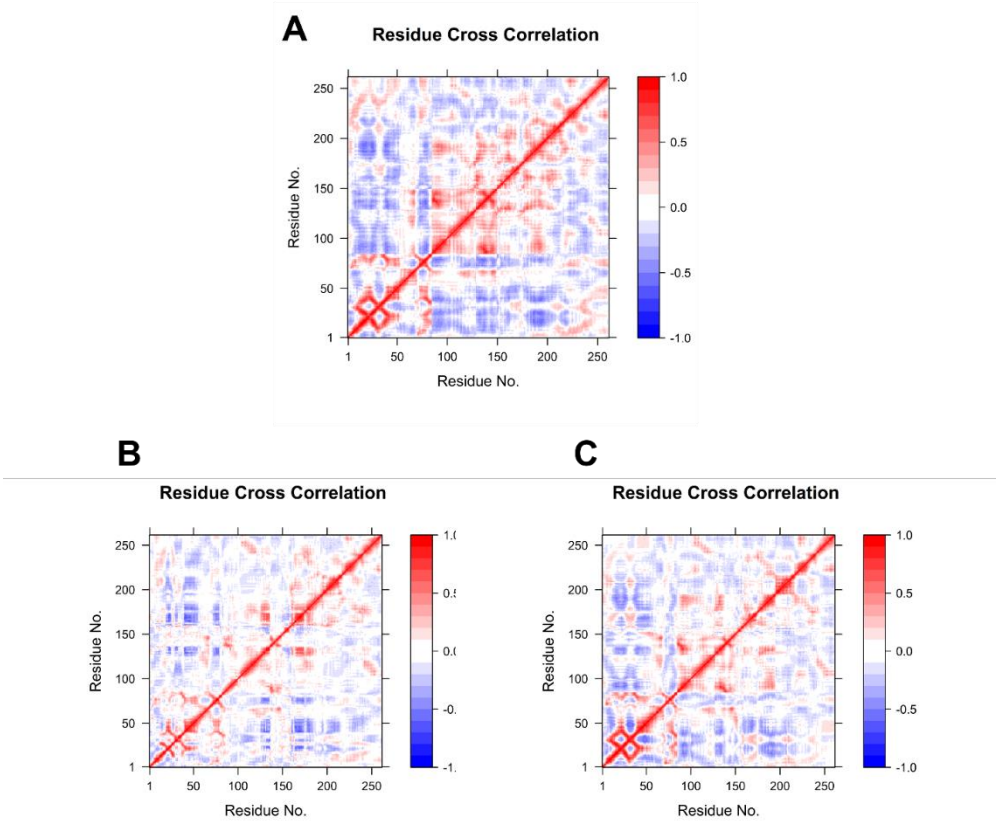

Figure 15. Dynamics cross-correlation matrix (DCCM). **(a)** Apoprotein; **(b)** Src kinase-AP23451 complex; **(c)** Src kinase-formononetin complex.

In the post-MD big data analysis, we used PCA to simplify and study the MD simulation trajectory. PCA helped us identify significant global movements in the Src kinase

protein during the 200 ns trajectory. When combined with DCCM analysis, PCA proved a powerful tool, as DCCM aids in understanding atomic movement and collective behavior within the protein-ligand complex, thereby helping elucidatets biological function [75]. A study by Akash *et al*. [76] on the in silico evaluation of anti-colorectal cancer inhibitors derived from resveratrol targeting the armadillo repeat domain of APC also employed PCA to reduce the dimensionality of MD simulation results from a 100 ns trajectory. PCA is useful for investigating high-dimensional data from MD simulations and transforming it into an informative low-dimensional space that simplifies the analysis of visual results. PCA is applied in MD simulations because they produce complex collective movements related to system stability and protein function over time (in this case, 200 ns). In this study, the large 200 ns trajectory produced diverse data, and PCA provided an analysis of various MD simulation parameters, simplifying the movements. Additionally, DCCM was used to analyze Calpha and the correlation between RMSD and DCCM [67].

4. Conclusions

This study employed *in silico* computational prediction to identify naringin as a promising Src-kinase inhibitor candidate among thirteen bioactive compounds derived from royal jelly, based on its binding energy, which closely approximated that of the reference inhibitor, AP2345. However, naringin was predicted to have poor pharmacokinetic properties through SwissADME evaluation, leading to the selection of formononetin as the most promising test compound. Formononetin exhibited favorable pharmacokinetic properties, with high GI absorption and druglikeness that complied with Lipinski's rules. Furthermore, it showed a favorable toxicity prediction. Formononetin interacts with the active-site amino acid residues of Src kinase via hydrogen bonding to Met341. DFT calculations showed a higher energy gap compared to the control inhibitor AP23451, indicating good stability. In the MD simulation, formononetin provided excellent stability to Src kinase, with predominant hydrophobic interactions after 200 ns, and the ligand conformation was calculated using RMSD, yielding a low value of 0.9945 Å. Through MM-PBSA calculations, we found that formononetin interacts well with Src kinase and maintains equilibrium distribution and conformational stability, while PCA and DCCM evaluations showed a positive correlation that validated the stability of the Src kinase-formononetin complex. These findings are valuable for proposing and considering future studies of royal jelly as a potential new anticancer agent. Laboratory validation of this research is required. Future work should prioritize experimental validation, including *in vitro* binding and enzymatic assays, followed by potential structure–activity optimization to refine potency and pharmacokinetic behavior. As a final note, this entire study constitutes a computational *in silico* prediction. Consequently, it cannot stand alone and requires further validation through subsequent investigations.

Author Contributions

Conceptualization, Y.A., G.M.G., D.A., and I.M.A.; methodology, Y.A., and G.M.G.; software, G.M.G., and I.M.A.; validation, Y.A., and G.M.G.; formal analysis, Y.A., G.M.G., D.A., S.S.S., C.H.W., A.M., T.K.W., R.P., I.W., and I.M.A.; investigation, G.M.G.; resources, Y.A., D.A., and I.M.A.; data curation, Y.A., G.M.G., D.A., and I.M.A.; writing—original draft preparation, Y.A., and G.M.G.; writing—review and editing, Y.A., G.M.G., D.A., S.S.S., C.H.W., A.M., T.K.W., R.P., I.W., and I.M.A.; visualization, G.M.G.; supervision, Y.A., D.A.,

and I.M.A.; project administration, Y.A.; funding acquisition, Y.A.. All authors have read and agreed to the published version of the manuscript.

Institutional Review Board Statement

Not applicable.

Informed Consent Statement

Not applicable.

Data Availability Statement

Data supporting the findings of this study are available upon reasonable request from the corresponding author.

Funding

The research was conducted with support from the *Riset Dan Inovasi Untuk Indonesia Maju* (RIIM) *Biologi Struktur Biomolekul Keanekaragaman Hayati* 2024 program (RIIM-ORHL 2-712266914168).

Acknowledgments

This work was carried out under the auspices of the Department of Biochemistry, IPB University, and the National Research and Innovation Agency. This work has received support from the *Riset Dan Inovasi Untuk Indonesia Maju* (RIIM) *Biologi Struktur Biomolekul Keanekaragaman Hayati* 2024 program (RIIM-ORHL 2-712266914168). The authors thank Dr. John Acton for his assistance at the manuscript preparation stage.

Conflicts of Interest

The authors declare no conflict of interest.

References

1. Anand, U.; Dey, A.; Chandel, A.K.S.; Sanyal, R.; Mishra, A.; Pandey, D.K.; De Falco, V.; Upadhyay, A.; Kandimalla, R.; Chaudhary, A.; Dhanjal, J.K.; Dewanjee, S.; Vallamkondu, J.; Pérez de la Lastra, J.M. Cancer chemotherapy and beyond: Current status, drug candidates, associated risks and progress in targeted therapeutics. *Genes Dis.* **2023**, *10*, 1367-1401, https://doi.org/10.1016/j.gendis.2022.02.007.
2. Yahya, E.B.; Alqadhi, A.M. Recent trends in cancer therapy: A review on the current state of gene delivery. *Life Sci.* **2021**, *269*, 119087, https://doi.org/10.1016/j.lfs.2021.119087.
3. Cao, W.; Qin, K.; Li, F.; Chen, W. Comparative study of cancer profiles between 2020 and 2022 using global cancer statistics (GLOBOCAN). *J. Natl. Cancer Cent.* **2024**, *4*, 128–134, https://doi.org/10.1016/j.jncc.2024.05.001.
4. Ucche, S.; Hayakawa, Y. Immunological Aspects of Cancer Cell Metabolism. *Int. J. Mol. Sci.* **2024**, *25*, 5288, https://doi.org/10.3390/ijms25105288.
5. Mahé, M.; Rios-Fuller, T.J.; Karolin, A.; Schneider, R.J. Genetics of enzymatic dysfunctions in metabolic disorders and cancer. *Front. Oncol.* **2023**, *13*, 1230934, https://doi.org/10.3389/fonc.2023.1230934.
6. Peng, S.; Fu, Y. FYN: emerging biological roles and potential therapeutic targets in cancer. *J. Transl. Med.* **2023**, *21*, 84, https://doi.org/10.1186/s12967-023-03930-0.
7. Pelaz, S.G.; Tabernero, A. Src: coordinating metabolism in cancer. *Oncogene* **2022**, *41*, 4917–4928, https://doi.org/10.1038/s41388-022-02487-4.

8. Ortiz, M.A.; Mikhailova, T.; Li, X.; Porter, B.A.; Bah, A.; Kotula, L. Src family kinases, adaptor proteins and the actin cytoskeleton in epithelial-to-mesenchymal transition. *Cell Commun. Signal* **2021**, *19*, 67, https://doi.org/10.1186/s12964-021-00750-x.
9. Voisset, E.; Brenet, F.; Lopez, S.; de Sepulveda, P. SRC-Family Kinases in Acute Myeloid Leukaemia and Mastocytosis. *Cancers* **2020**, *12*, 1996, https://doi.org/10.3390/cancers12071996.
10. Luo, J.; Zou, H.; Guo, Y.; Tong, T.; Ye, L.; Zhu, C.; Deng, L.; Wang, B.; Pan, Y.; Li, P. SRC kinase-mediated signaling pathways and targeted therapies in breast cancer. *Breast Cancer Res.* **2022**, *24*, 99, https://doi.org/10.1186/s13058-022-01596-y.
11. Lieu, C.; Kopetz, S. The Src Family of Protein Tyrosine Kinases: A New and Promising Target for Colorectal Cancer Therapy. *Clin. Colorectal Cancer* **2010**, *9*, 89–94, https://doi.org/10.3816/CCC.2010.n.012.
12. Zhang, S.; Yu, D. Targeting Src family kinases in anti-cancer therapies: turning promise into triumph. *Trends Pharmacol. Sci.* **2012**, *33*, 122–128, https://doi.org/10.1016/j.tips.2011.11.002.
13. Martellucci, S.; Clementi, L.; Sabetta, S.; Mattei, V.; Botta, L.; Angelucci, A. Src Family Kinases as Therapeutic Targets in Advanced Solid Tumors: What We Have Learned So Far. *Cancers* **2020**, *12*, 1448, https://doi.org/10.3390/cancers12061448.
14. Debela, D.T.; Muzazu, S.G.Y.; Heraro, K.D.; Ndalama, M.T.; Mesele, B.W.; Haile, D.C.; Kitui, S.K.; Manyazewal, T. New approaches and procedures for cancer treatment: Current perspectives. *SAGE Open Med.* **2021**, *9*, 20503121211034366, https://doi.org/10.1177/20503121211034366.
15. Xiong, R.-G.; Huang, S.-Y.; Wu, S.-X.; Zhou, D.-D.; Yang, Z.-J.; Saimaiti, A.; Zhao, C.-N.; Shang, A.; Zhang, Y.-J.; Gan, R.-Y.; Li, H.-B. Anticancer Effects and Mechanisms of Berberine from Medicinal Herbs: An Update Review. *Molecules* **2022**, *27*, 4523, https://doi.org/10.3390/molecules27144523.
16. Lee, H.Y.J.; Meng, M.; Liu, Y.; Su, T.; Kwan, H.Y. Medicinal herbs and bioactive compounds overcome the drug resistance to epidermal growth factor receptor inhibitors in non-small cell lung cancer (Review). *Oncol. Lett.* **2021**, *22*, 646, https://doi.org/10.3892/ol.2021.12907.
17. Salama, S.; Shou, Q.; Abd El-Wahed, A.A.; Elias, N.; Xiao, J.; Swillam, A.; Umair, M.; Guo, Z.; Daglia, M.; Wang, K.; Khalifa, S.A.M.; El-Seedi, H.R. Royal Jelly: Beneficial Properties and Synergistic Effects with Chemotherapeutic Drugs with Particular Emphasis in Anticancer Strategies. *Nutrients* **2022**, *14*, 4166, https://doi.org/10.3390/nu14194166.
18. Aparecida dos Santos France, F.; Maeda, D.K.; Rodrigues, A.B.; Ono, M.; Lopes Nogueira Marchetti, F.; Marchetti, M.M.; Faustino Martins, A.C.; Gomes, R.d.S.; Rainho, C.A. Exploring fatty acids from royal jelly as a source of histone deacetylase inhibitors: from the hive to applications in human well-being and health. *Epigenetics* **2024**, *19*, 2400423, https://doi.org/10.1080/15592294.2024.2400423.
19. Bălan, A.; Moga, M.A.; Dima, L.; Toma, S.; Elena Neculau, A.; Anastasiu, C.V. Royal Jelly—A Traditional and Natural Remedy for Postmenopausal Symptoms and Aging-Related Pathologies. *Molecules* **2020**, *25*, 3291, https://doi.org/10.3390/molecules25143291.
20. Kumar, R.; Thakur, A.; Kumar, S.; Hajam, Y.A. Royal jelly a promising therapeutic intervention and functional food supplement: A systematic review. *Heliyon* **2024**, *10*, e37138, https://doi.org/10.1016/j.heliyon.2024.e37138.
21. Fratini, F.; Cilia, G.; Mancini, S.; Felicioli, A. Royal Jelly: An ancient remedy with remarkable antibacterial properties. *Microbiol. Res.* **2016**, *192*, 130–141, https://doi.org/10.1016/j.micres.2016.06.007.
22. Collazo, N.; Carpena, M.; Nuñez-Estevez, B.; Otero, P.; Simal-Gandara, J.; Prieto, M.A. Health Promoting Properties of Bee Royal Jelly: Food of the Queens. *Nutrients* **2021**, *13*, 543, https://doi.org/10.3390/nu13020543.
23. Sönmez, E. Royal Jelly in modern biomedicine: A review of its bioactive constituents and health benefits. *J. Funct. Foods* **2025**, *134*, 107062, https://doi.org/10.1016/j.jff.2025.107062.
24. Khamouli, S.; Rehman, M.T.; Zegheb, N.; Hussain, A.; Khan, M.A. Comprehensive in silico discovery of c-Src tyrosine kinase inhibitors in cancer treatment: a unified approach combining pharmacophore modeling, 3D QSAR, DFT, and molecular dynamics simulation. *J. King Saud Univ. Sci.* **2024**, *36*, 103076, https://doi.org/10.1016/j.jksus.2023.103076.
25. Colovos, C.; Yeates, T.O. Verification of protein structures: Patterns of nonbonded atomic interactions. *Protein Sci.* **1993**, *2*, 1511–1519, https://doi.org/10.1002/pro.5560020916.
26. Lüthy, R.; Bowie, J.U.; Eisenberg, D. Assessment of protein models with three-dimensional profiles. *Nature* **1992**, *356*, 83-85, https://doi.org/10.1038/356083a0.
27. Sippl, M.J. Recognition of errors in three-dimensional structures of proteins. *Protein Struct. Funct. Bioinform.* **1993**, *17*, 355–362, https://doi.org/10.1002/prot.340170404.

28. Wiederstein, M.; Sippl, M.J. ProSA-web: interactive web service for the recognition of errors in three-dimensional structures of proteins. *Nucleic Acids Res.* **2007**, *35*, W407–W410, https://doi.org/10.1093/nar/gkm290.
29. El-Seedi, H.R.; Salama, S.; El-Wahed, A.A.A.; Guo, Z.; Di Minno, A.; Daglia, M.; Li, C.; Guan, X.; Buccato, D.G.; Khalifa, S.A.M.; Wang, K. Exploring the Therapeutic Potential of Royal Jelly in Metabolic Disorders and Gastrointestinal Diseases. *Nutrients* **2024**, *16*, 393, https://doi.org/10.3390/nu16030393.
30. Botezan, S.; Baci, G.-M.; Bagameri, L.; Pașca, C.; Dezmirean, D.S. Current Status of the Bioactive Properties of Royal Jelly: A Comprehensive Review with a Focus on Its Anticancer, Anti-Inflammatory, and Antioxidant Effects. *Molecules* **2023**, *28*, 1510, https://doi.org/10.3390/molecules28031510.
31. Land, H.; Humble, M.S. YASARA: A Tool to Obtain Structural Guidance in Biocatalytic Investigations. In Protein Engineering: Methods and Protocols; Bornscheuer, U.T., Höhne, M., Eds.; Springer New York: New York, NY, **2018**; Volume 1685, pp. 43-67, https://doi.org/10.1007/978-1-4939-7366-8_4.
32. Krieger, E.; Vriend, G. YASARA View—molecular graphics for all devices—from smartphones to workstations. *Bioinformatics* **2014**, *30*, 2981–2982, https://doi.org/10.1093/bioinformatics/btu426.
33. Krieger, E.; Vriend, G. New ways to boost molecular dynamics simulations. *J. Comput. Chem.* **2015**, *36*, 996–1007, https://doi.org/10.1002/jcc.23899.
34. Krieger, E.; Koraimann, G.; Vriend, G. Increasing the precision of comparative models with YASARA NOVA—a self-parameterizing force field. *Protein Struct. Funct. Bioinform.* **2002**, *47*, 393–402, https://doi.org/10.1002/prot.10104.
35. Wang, S.; Xie, J.; Pei, J.; Lai, L. CavityPlus 2022 Update: An Integrated Platform for Comprehensive Protein Cavity Detection and Property Analyses with User-friendly Tools and Cavity Databases. *J. Mol. Biol.* **2023**, *435*, 168141, https://doi.org/10.1016/j.jmb.2023.168141.
36. Banerjee, P.; Kemmler, E.; Dunkel, M.; Preissner, R. ProTox 3.0: a webserver for the prediction of toxicity of chemicals. *Nucleic Acids Res.* **2024**, *52*, W513-W520, https://doi.org/10.1093/nar/gkae303.
37. Rauf, A.; Khan, H.; Khan, M.; Abusharha, A.; Serdaroğlu, G.; Daglia, M. In Silico, SwissADME, and DFT Studies of Newly Synthesized Oxindole Derivatives Followed by Antioxidant Studies. *J. Chem.* **2023**, *2023*, 5553913, https://doi.org/10.1155/2023/5553913.
38. Ibrahim, M.A.A.; Abdeljawaad, K.A.A.; Roshdy, E.; Mohamed, D.E.M.; Ali, T.F.S.; Gabr, G.A.; Jaragh-Alhadad, L.A.; Mekhemer, G.A.H.; Shawky, A.M.; Sidhom, P.A.; Abdelrahman, A.H.M. In silico drug discovery of SIRT2 inhibitors from natural source as anticancer agents. *Sci. Rep.* **2023**, *13*, 2146, https://doi.org/10.1038/s41598-023-28226-7.
39. Filimonov, D.A.; Lagunin, A.A.; Gloriozova, T.A.; Rudik, A.V.; Druzhilovskii, D.S.; Pogodin, P.V.; Poroikov, V.V. Prediction of the Biological Activity Spectra of Organic Compounds Using the Pass Online Web Resource. *Chem. Heterocycl. Compd.* **2014**, *50*, 444–457, https://doi.org/10.1007/s10593-014-1496-1.
40. Akhter, S.; Concepcion, O.; de la Torre, A.F.; Ali, A.; Raza, A.R.; Eman, R.; Khalid, M.; Rehman, M.F.u.; Akram, M.S.; Ali, H.M. Synthesis, spectroscopic characterization, DFT and molecular dynamics of quinoline-based peptoids. *Arab. J. Chem.* **2023**, *16*, 104570, https://doi.org/10.1016/j.arabjc.2023.104570.
41. Joseph Sahayarayan, J.; Soundar Rajan, K.; Nachiappan, M.; Prabhu, D.; Guru Raj Rao, R.; Jeyakanthan, J.; Hossam Mahmoud, A.; Mohammed, O.B.; Morgan, A.M.A. Identification of potential drug target in malarial disease using molecular docking analysis. *Saudi J. Biol. Sci.* **2020**, *27*, 3327-3333, https://doi.org/10.1016/j.sjbs.2020.10.019.
42. Ibrahim, M.A.A.; Abdeljawaad, K.A.A.; Abdelrahman, A.H.M.; Arzumanyan, G.; Mekhemer, G.A.H.; Abdelbacki, A.M.M.; Sidhom, P.A.; Sayed, S.R.M.; Hegazy, M.-E.F. Hunting potential SIRT2 inhibitors towards cancer treatment: Drug repurposing, molecular dynamics, and binding energy computations. *Biochem. Biophys. Res. Commun.* **2025**, *760*, 151701, https://doi.org/10.1016/j.bbrc.2025.151701.
43. Rathod, S.; Shinde, K.; Porlekar, J.; Choudhari, P.; Dhavale, R.; Mahuli, D.; Tamboli, Y.; Bhatia, M.; Haval, K.P.; Al-Sehemi, A.G.; Pannipara, M. Computational Exploration of Anti-cancer Potential of Flavonoids against Cyclin-Dependent Kinase 8: An *In Silico* Molecular Docking and Dynamic Approach. *ACS Omega* **2023**, *8*, 391-409, https://doi.org/10.1021/acsomega.2c04837.
44. Skjærven, L.; Yao, X.-Q.; Scarabelli, G.; Grant, B.J. Integrating protein structural dynamics and evolutionary analysis with Bio3D. *BMC Bioinformatics* **2014**, *15*, 399, https://doi.org/10.1186/s12859-014-0399-6.
45. Ezaj, M.M.A.; Junaid, M.; Akter, Y.; Nahrin, A.; Siddika, A.; Afrose, S.S.; Nayeem, S.M.A.; Haque, M.S.; Moni, M.A.; Hosen, S.M.Z. Whole proteome screening and identification of potential epitopes of SARS-CoV-2 for vaccine design-an immunoinformatic, molecular docking and molecular dynamics simulation

accelerated robust strategy. *J. Biomol. Struct. Dyn.* **2022**, *40*, 6477-6502, https://doi.org/10.1080/07391102.2021.1886171.
46. Grant, B.J.; Skjærven, L.; Yao, X.-Q. The Bio3D packages for structural bioinformatics. *Protein Sci.* **2021**, *30*, 20–30, https://doi.org/10.1002/pro.3923.
47. Naveed, M.; Batool, Z.; Aziz, T.; Javed, K.; Ali, N.; Rehman, H.M.; Alharbi, M.; Alasmari, A.F.; Alshammari, A. An in silico approach uncovering the competency of oncolytic human adenovirus 52 for targeted breast cancer virotherapy. *Sci. Rep.* **2024**, *14*, 26405, https://doi.org/10.1038/s41598-024-77664-4.
48. Khalid, Z.; Khan, A.T.-A.; Alnajjar, R.; Santali, E.; Shakoori, A.R. In silico mutational analysis of ACE2 to check the susceptibility of lung cancer patients towards COVID-19. *Sci. Rep.* **2022**, *12*, 7798, https://doi.org/10.1038/s41598-022-11805-5.
49. Priyadarshini, G.; Sukumaran, G.; Dilipan, E.; Ramani, P. Targeting Oral Cancer: In Silico Docking Studies of Phytochemicals on Oncogenic Molecular Markers. *Asian Pac. J. Cancer Prev.* **2024**, *25*, 2069-2075, https://doi.org/10.31557/APJCP.2024.25.6.2069.
50. Yavari, P.; Roointan, A.; Naghdibadi, M.; Masoudi-Sobhanzadeh, Y. In-silico identification of therapeutic targets in pancreatic ductal adenocarcinoma using WGCNA and *Trader*. *Sci. Rep.* **2024**, *14*, 23292, https://doi.org/10.1038/s41598-024-74252-4.
51. Tomić, D.; Murgić, J.; Fröbe, A.; Skala, K.; Vrljičak, A.; Medved Rogina, B.; Kolarek, B.; Bojović, V. Exploring potential therapeutic combinations for castration-sensitive prostate cancer using supercomputers: a proof of concept study. *Sci. Rep.* **2024**, *14*, 18824, https://doi.org/10.1038/s41598-024-69880-9.
52. Sawal, H.A.; Nighat, S.; Safdar, T.; Anees, L. Comparative In Silico Analysis and Functional Characterization of TANK-Binding Kinase 1–Binding Protein 1. *Bioinform. Biol. Insights* **2023**, *17*, 11779322231164828, https://doi.org/10.1177/11779322231164828.
53. Chandrasekaran, G.; Hwang, E.C.; Kang, T.W.; Kwon, D.D.; Park, K.; Lee, J.-J.; Lakshmanan, V.-K. Computational Modeling of complete HOXB13 protein for predicting the functional effect of SNPs and the associated role in hereditary prostate cancer. *Sci. Rep.* **2017**, *7*, 43830, https://doi.org/10.1038/srep43830.
54. Sun, X.; Liu, Y.; Ma, T.; Zhu, N.; Lao, X.; Zheng, H. DCTPep, the data of cancer therapy peptides. *Sci. Data* **2024**, *11*, 541, https://doi.org/10.1038/s41597-024-03388-9.
55. Aljuaid, A.; Salam, A.; Almehmadi, M.; Baammi, S.; Alshabrmi, F.M.; Allahyani, M.; Al-Zaydi, K.M.; Izmirly, A.M.; Almaghrabi, S.; Baothman, B.K.; Shahab, M. Structural Homology-Based Drug Repurposing Approach for Targeting NSP12 SARS-CoV-2. *Molecules* **2022**, *27*, 7732, https://doi.org/10.3390/molecules27227732.
56. Yang, J.; Roy, A.; Zhang, Y. Protein–ligand binding site recognition using complementary binding-specific substructure comparison and sequence profile alignment. *Bioinformatics* **2013**, *29*, 2588–2595, https://doi.org/10.1093/bioinformatics/btt447.
57. Venkatesh, G.; Mammadova, K.; Vennila, P.; Mishma, J.N.C.; Premkumar, R.; Kaya, S. Green synthesis of novel amino acid-coupled 1, 2, 4-triazoles derivatives using lemon juice as a green catalyst: Potential antiproliferative, antimicrobial, DFT computation and molecular docking analysis. *J. Mol. Struct.* **2026**, *1351*, 144187, https://doi.org/10.1016/j.molstruc.2025.144187.
58. Ravikumar, Y.; Koonyosying, P.; Srichairatanakool, S.; Ponpandian, L.N.; Kumaravelu, J.; Srichairatanakool, S. In Silico Molecular Docking and Dynamics Simulation Analysis of Potential Histone Lysine Methyl Transferase Inhibitors for Managing β-Thalassemia. *Molecules* **2023**, *28*, 7266, https://doi.org/10.3390/molecules28217266.
59. Abdul-Hammed, M.; Adedotun, I.O.; Falade, V.A.; Adepoju, A.J.; Olasupo, S.B.; Akinboade, M.W. Target-based drug discovery, ADMET profiling and bioactivity studies of antibiotics as potential inhibitors of SARS-CoV-2 main protease (M^{pro}). *VirusDisease* **2021**, *32*, 642-656, https://doi.org/10.1007/s13337-021-00717-z.
60. Daina, A.; Michielin, O.; Zoete, V. SwissADME: a free web tool to evaluate pharmacokinetics, drug-likeness and medicinal chemistry friendliness of small molecules. *Sci. Rep.* **2017**, *7*, 42717, https://doi.org/10.1038/srep42717.
61. Mendie, L.E.; Hemalatha, S. Molecular Docking of Phytochemicals Targeting GFRs as Therapeutic Sites for Cancer: an In Silico Study. *Appl. Biochem. Biotechnol.* **2022**, *194*, 215–231, https://doi.org/10.1007/s12010-021-03791-7.
62. Agu, P.C.; Afiukwa, C.A.; Orji, O.U.; Ezeh, E.M.; Ofoke, I.H.; Ogbu, C.O.; Ugwuja, E.I.; Aja, P.M. Molecular docking as a tool for the discovery of molecular targets of nutraceuticals in diseases management. *Sci. Rep.* **2023**, *13*, 13398, https://doi.org/10.1038/s41598-023-40160-2.

63. Chen, X.; Li, X.; Li, Y. Toxicity inhibition strategy of microplastics to aquatic organisms through molecular docking, molecular dynamics simulation and molecular modification. *Ecotoxicol. Environ. Saf.* **2021**, *226*, 112870, https://doi.org/10.1016/j.ecoenv.2021.112870.
64. C, S.; S, D.K.; Ragunathan, V.; Tiwari, P.; A, S.; P, B.D. Molecular docking, validation, dynamics simulations, and pharmacokinetic prediction of natural compounds against the SARS-CoV-2 main-protease. *J. Biomol. Struct. Dyn.* **2022**, *40*, 585-611, https://doi.org/10.1080/07391102.2020.1815584.
65. Uzzaman, M.; Hasan, M.K.; Mahmud, S.; Yousuf, A.; Islam, S.; Uddin, M.N.; Barua, A. Physicochemical, spectral, molecular docking and ADMET studies of Bisphenol analogues; A computational approach. *Informat. Med. Unlocked* **2021**, *25*, 100706, https://doi.org/10.1016/j.imu.2021.100706.
66. Cavasotto, C.N.; Aucar, M.G. High-Throughput Docking Using Quantum Mechanical Scoring. *Front. Chem.* **2020**, *8*, 246, https://doi.org/10.3389/fchem.2020.00246.
67. Holikulov, U.; Khodiev, M.; Issaoui, N.; Jumabaev, A.; Kumar, N.; Al-Dossary, O.M. Exploring the non-covalent interactions, vibrational and electronic properties of 2-methyl-4-hydro-1,3,4-triazol-thione-5 in different solutions. *J. King Saud. Univ. Sci.* **2024**, *36*, 103164, https://doi.org/10.1016/j.jksus.2024.103164.
68. Ewell, S.M.; Burton, H.; Mochona, B. In Silico Screening of 1,3,4-Thiadiazole Derivatives as Inhibitors of Vascular Endothelial Growth Factor Receptor-2 (VEGFR-2). *Curr. Issues Mol. Biol.* **2024**, *46*, 11220-11235, https://doi.org/10.3390/cimb46100666.
69. Irsal, R.A.P.; Gholam, G.M.; Dwicesaria, M.A.; Mansyah, T.F.; Chairunisa, F. Computational exploration of palmitoyl-protein thioesterase 1 inhibition by *Juniperus phoenicea* L. for anti-dementia treatment. *J. Taibah Univ. Med. Sci.* **2024**, *19*, 1165-1180, https://doi.org/10.1016/j.jtumed.2024.12.005.
70. Eisa, A.A. Insights into novel inhibitory compounds against 14–3-3 ε potential cancer therapeutic target through microscopic solvated dynamics. *J. Mol. Liq.* **2025**, *428*, 127541, https://doi.org/10.1016/j.molliq.2025.127541.
71. Genheden, S.; Ryde, U. The MM/PBSA and MM/GBSA methods to estimate ligand-binding affinities. *Expert Opin. Drug Discov.* **2015**, *10*, 449–461, https://doi.org/10.1517/17460441.2015.1032936.
72. Thakur, Y.; Pande, R. Exploration of *In-silico* screening of therapeutic agents against SARS-CoV-2. *Chem. Phys.* **2021**, *551*, 111354, https://doi.org/10.1016/j.chemphys.2021.111354.
73. Dasmahapatra, U.; Kumar, C.K.; Das, S.; Subramanian, P.T.; Murali, P.; Isaac, A.E.; Ramanathan, K.; Mm, B.; Chanda, K. *In-silico* molecular modelling, MM/GBSA binding free energy and molecular dynamics simulation study of novel pyrido fused imidazo[4,5-*c*]quinolines as potential anti-tumor agents. *Front. Chem.* **2022**, *10*, 991369, https://doi.org/10.3389/fchem.2022.991369.
74. Rolta, R.; Salaria, D.; Fadare, O.A.; Kaur, G.; Fadare, R.Y.; Prakash, A.; Kaman, L.; Medhi, B. Investigation of phytoconstituents interactions with human Src kinase in a bid to improve cholangiocarcinoma chemotherapy: An *in-silico* approach. *Biochem. Biophys. Res. Commun.* **2025**, *787*, 152733, https://doi.org/10.1016/j.bbrc.2025.152733.
75. Sharanya, C.S.; Wilbee, D.S.; Sathi, S.N.; Natarajan, K. Computational screening combined with well-tempered metadynamics simulations identifies potential TMPRSS2 inhibitors. *Sci. Rep.* **2024**, *14*, 16197, https://doi.org/10.1038/s41598-024-65296-7.
76. Akash, S.; Islam, M.R.; Bhuiyan, A.A.; Islam, M.N.; Bayıl, I.; Saleem, R.M.; Albadrani, G.M.; Al-Ghadi, M.Q.; Abdel-Daim, M.M. *In silico* evaluation of anti-colorectal cancer inhibitors by Resveratrol derivatives targeting Armadillo repeats domain of APC: molecular docking and molecular dynamics simulation. *Front. Oncol.* **2024**, *14*, 1360745, https://doi.org/10.3389/fonc.2024.1360745.

Publisher's Note & Disclaimer